AIAA JOURNAL
Vol. 46, No. 10, October 2008

Numerical Investigations of Reignition in Vortex-Perturbed *n*-Heptane Nonpremixed Flames

Rishikesh Venugopal* and John Abraham†
Purdue University, West Lafayette, Indiana 47907

DOI: 10.2514/1.35094

Numerical investigations of reignition in *n*-heptane nonpremixed flames perturbed by counter-rotating vortex pairs are performed. The conditions simulated are representative of high-pressure combustion chambers with high-Reynolds-number jet flames. A two-dimensional numerical formulation that employs sixth-order spatial accuracy and fourth-order time integration is used to solve the governing equations for compressible, viscous, and reacting flows. The oxidation of *n*-heptane is modeled using a 34-species mechanism involving 56 reaction steps. Transport is modeled using the unity Lewis number and the mixture-averaged models. For the conditions simulated, reignition occurs through lateral diffusion of species and heat from the adjoining edge flames to the quenched regions and hence cannot be predicted by one-dimensional flamelet models. Following reconnection of the diffusion flame, a vortical pocket travels on the fuel side and acts as a major source of combustion products such as CO and H_2. The results show that whereas an increase in the vortex velocity scale results in higher rates of reignition and product formation, an increase in the length scale decreases the rate of reignition and increases the amount of products formed in the vortical pocket. The choice of the transport formulation has a minor influence on the predicted flame temperatures and major species concentrations.

Nomenclature

c	=	progress variable
c_p	=	mixture specific heat
D_k	=	mass diffusivity of the kth species
D_{km}	=	mixture-averaged diffusivity of the kth species
d_v	=	initial diameter of the vortex pair
h_k	=	specific enthalpy of species k
h_k^0	=	standard enthalpy of formation of species k
l_r	=	length-scale ratio
p	=	pressure
Re	=	vortex Reynolds number
T	=	temperature
u_e	=	specific internal energy
u_i	=	velocity in the ith Cartesian direction
u_v	=	initial convection velocity of the vortex pair
$\dot{w}_k$	=	chemical production/destruction rate of species k
x_i	=	distance in the ith Cartesian direction
Y_k	=	mass fraction of the kth species
Z	=	mixture fraction
λ	=	mixture thermal conductivity
μ	=	dynamic viscosity of the mixture
ρ	=	mass density of the mixture
τ_c	=	representative chemical time scale for the unperturbed flame
τ_r	=	time-scale ratio
χ	=	instantaneous scalar dissipation rate
χ_e	=	steady extinction limit for a laminar diffusion flame
χ_r	=	ratio of χ_{st} to χ_e
χ_{st}	=	instantaneous scalar dissipation rate at the stoichiometric mixture fraction

Received 12 October 2007; accepted for publication 24 April 2008.

*Graduate Research Assistant, School of Mechanical Engineering, 500 Allison Road. Student Member AIAA.

†Professor, School of Mechanical Engineering, 500 Allison Road. Senior Member AIAA.

I. Introduction

TURBULENT jet diffusion flames form an important class of reacting flows as they occur in practical combustion devices, such as direct-injection diesel engines, and gas turbines. Over the past four decades, significant progress has been made in the understanding and prediction of the structure of combusting jets [1–3]. However, the majority of the experimental and numerical studies have focused on the jet flame structure in the far field, and turbulence-chemistry interactions in the near field ($x/d < 30$) are poorly understood. In the case of jet flames occurring in diesel chambers, near-field phenomena could impact flame stability and pollutant formation. For instance, flame liftoff in diesel jets is an example of a near-field phenomenon that has received considerable attention in recent years [4–6] and has been shown to influence pollutant formation through fuel/air premixing before combustion [7]. Recent Reynolds-averaged Navier–Stokes (RANS) modeling approaches employing different models such as diffusion flamelets [8] and perfectly stirred reactors [9] predict experimentally observed diesel flame liftoff heights within a certain range of chamber conditions. However, such approaches lack generality and ignore effects due to unsteadiness and curvature on the local flame structure. Moreover, as discussed in our recent review [6], near-field phenomena such as liftoff can occur through a combination of mechanisms, which renders RANS approaches with a presumed turbulence–chemistry interaction inappropriate.

Direct numerical simulation (DNS), on the other hand, offers great potential in exploring the underlying physical mechanisms for near-field phenomena, as no a priori assumptions about the local flame structure are made. Recently, there have been attempts in the literature to directly simulate the near field of jet flames [10,11] with simplified chemistry and at relatively low jet Reynolds numbers ($Re < 10,000$). These studies show that local extinction and reignition phenomena are prevalent in the near field. Nevertheless, a detailed understanding of these phenomena for practical jet Reynolds numbers is lacking. Flame extinction has received more attention relative to reignition through experimental and numerical means [12]. Hence, the emphasis of our work is on reignition.

DNS of jet flames at Reynolds numbers encountered in gas turbines and diesel engines ($\sim 10^5$) is impractical even with simplified chemistry, but studies in more simplified and canonical configurations such as isotropic decaying turbulence, turbulent mixing layers, and flame–vortex interactions are affordable and can provide useful insights into near-field flame dynamics. In this work,

we choose the flame–vortex setup to explore reignition under high-pressure, high-Reynolds-number conditions. Because of its configurational simplicity, the flame–vortex setup allows the incorporation of multistep chemistry without prohibitive computational costs and allows the isolation of unsteady and curvature effects. A comprehensive review of flame–vortex studies focusing on flame surface enhancement and extinction in both premixed and nonpremixed configurations, primarily under atmospheric pressure and low-Reynolds-number conditions, can be found in [13]. In the subsequent discussion, we will focus on the current understanding of reignition in nonpremixed configurations.

In a turbulent jet flame, local extinction can occur due to excursions of the instantaneous scalar dissipation rate χ above the extinction limit χ_e [14]. The recent incompressible DNS study by Sripakagorn et al. [15] of a diffusion flame evolving in isotropic decaying turbulence with single-step idealized chemistry shows that reignition can occur through three modes following local extinction. When the excursions of χ above χ_e are small and short-lived, reignition occurs through an independent flamelet scenario in which extinguished regions reignite without any interactions with neighboring burning regions. On the other hand, when the excursions of χ are large and last for a relatively long time, reignition can occur either through the propagation of edge flames [16] or through engulfment of the extinguished region by neighboring hot gases. For the conditions simulated by Sripakagorn et al. [15], the latter two modes of reignition were found to be dominant.

The importance of edge-flame dynamics during reignition has also been demonstrated in the DNS study of a planar methane jet flame by Pantano [10]. The jet Reynolds number simulated was 3000 and a 4-step reduced mechanism [17] was employed. The analysis showed that the propagation rates of the edge flames were strongly influenced by the evolution of χ in the reigniting regions. Although values of χ higher than χ_e caused the flame edges to recede away from the extinguished regions in the form of extinction fronts, the edge flames propagated toward the extinguished regions as ignition fronts, leading to reignition as χ relaxed to values lower than χ_e. These observations are consistent with the experiments of Santoro et al. [18] in counterflow mixing layers.

Reignition has been investigated, to a limited extent, through studies of flame–vortex interactions. Santoro et al. [19] experimentally investigated extinction and reignition in vortex-perturbed counterflow methanol flames. The vortex Reynolds numbers were relatively low ($Re < 100$) and, following local disruption of the flame front, the resulting flame edges were found to propagate and reestablish the diffusion flame. Recently, Hermanns et al. [20] performed a numerical investigation of edge-flame dynamics in diffusion-flame–vortex interactions. The diffusion flame was represented by a flame sheet and the constant-density approximation was invoked. Transport properties such as viscosity and thermal diffusivity were also assumed to be constant. The model results showed that when strong vortices interacted with robust flames, axial extinction followed by reignition occurred and the dynamics of the edge flames were predominantly controlled by vortex-induced convective velocities. However, in the case of weak vortices, the model failed to predict the viscous dissipation of the vortex upon contact with hot gases in the flame due to the constant-property assumption. Moreover, the presumed form of the edge-flame speed did not account for mutual interactions between edge flames, which could be important during reignition. Evidence of such interactions will be shown in our study.

Although the effects of unsteadiness and curvature on reignition are not well understood, studies in the literature [21,22] have explored curvature effects in relation to differential diffusion in vortex-perturbed diluted hydrogen–air nonpremixed flames. Both air-side and fuel-side vortices have been considered, which give rise to flame curvature of opposite signs (convex/concave). For instance, the flame–vortex studies of Yoshida and Takagi [21] show that the tendency to reignite may be different for fuel-side and air-side vortices, due to differential diffusion of H_2 with respect to other species such as N_2. In the present work, we characterize the vortex-induced flame curvature in terms of the vortex size, and we focus on the influence of curvature on the mechanism of reignition, in addition to exploring differential diffusion effects.

In addition to single-vortex–flame interactions, recent experimental and numerical studies [23,24] have focused on double-vortex–flame interactions, in which two counterpropagating vortex pairs from the fuel and the air sides are allowed to impinge on an initially flat flame. In [24], a numerical model based on a modified vorticity–velocity formulation with reduced chemistry and transport was employed to investigate the time-dependent structure of methane–air counterflow flames undergoing extinction and reignition in a double-vortex configuration. The results confirmed the presence of a negative edge-flame speed many times greater than the premixed laminar flame speed soon after the vortices caused local extinction. Subsequently, the edges transformed into ignition fronts and propagated with a speed comparable to the laminar flame speed to reignite the quenched regions. A premixedness index measuring the angle between the local gradients of fuel and oxidizer was employed to quantify the degree of premixing during reignition.

In the section that follows, we outline the objectives and contributions of the present work. Then a brief discussion of the governing equations, numerical methods, and chemical kinetic mechanism is presented in Sec. III. Results and discussion follow in Sec. IV. The paper ends with a summary and conclusions in Sec. V.

II. Objectives and Contributions of This Work

In this work, we perform 2-D numerical investigations of reignition in flame–vortex interactions under high-pressure, high-Reynolds-number conditions with multistep chemical kinetics and multicomponent-species transport. Our focus is on pressures of about 40 bar, oxidizer temperatures of about 1000 K, and relatively large density ratios between the fuel and the oxidizer ($\sim$8). There are no previous flame–vortex-interaction studies in the literature under these conditions. A common employed surrogate, *n*-heptane, for practical fuels such as diesel is chosen as the fuel, and its oxidation chemistry is represented by a 34-species mechanism involving 56 reaction steps [25]. We consider relatively large chemical-to-vortex time-scale ratios up to 1650, in order to emulate the interactions of strong vortices with flamelets that could occur in the near field of high-Reynolds-number jet flames. Previous studies in the literature [19,24,26,27] have considered values of, at most, 60. The vortex Reynolds numbers employed are relatively high (175–900) and are chosen to represent the turbulent integral-scale Reynolds numbers in the near field ($x/d < 30$) of jets with inlet Reynolds numbers in the range of 50,000–400,000. We address questions related to the nature of flow–chemistry interactions during reignition and the influence of unsteadiness and curvature on the rate of reignition (flame-stability) and product formation. The implications of the observed interaction outcomes for turbulent combustion modeling are also discussed.

III. Numerical Formulation

A. Governing Equations and Numerical Methods

In this work, we employ the Flow, Large-Eddy, and Direct Simulation (FLEDS) code [28–30] to solve the following governing equations for compressible, viscous, and reacting flows:

$$\frac{\partial \rho}{\partial t} + \frac{\partial}{\partial x_j}(\rho u_j) = 0 \tag{1}$$

$$\frac{\partial}{\partial t}(\rho u_i) + \frac{\partial}{\partial x_j}(\rho u_i u_j) = -\frac{\partial p}{\partial x_i} + \frac{\partial \sigma_{ij}}{\partial x_j} \tag{2}$$

$$\frac{\partial}{\partial t}(\rho Y_k) + \frac{\partial}{\partial x_j}(\rho Y_k u_j) = \frac{\partial}{\partial x_j}\left(\rho D_k \frac{\partial Y_k}{\partial x_j}\right) + \dot{w}_k \tag{3}$$

$$\frac{\partial}{\partial t}(\rho e) + \frac{\partial}{\partial x_j}[(\rho e + p)u_j] = \frac{\partial}{\partial x_j}(\sigma_{ij}u_j) + \frac{\partial}{\partial x_j}\left(\lambda \frac{\partial T}{\partial x_j}\right) + \frac{\partial}{\partial x_j}\left[\rho \sum_k \left(h_k D_k \frac{\partial Y_k}{\partial x_j}\right)\right] + \sum_k \dot{w}_k h_k^0 \quad (4)$$

In Eq. (2), σ_{ij} is the viscous stress tensor, given by

$$\sigma_{ij} = \mu\left[\left(\frac{\partial u_i}{\partial x_j} + \frac{\partial u_j}{\partial x_i}\right) - \frac{2}{3}\frac{\partial u_k}{\partial x_k}\delta_{ij}\right] \quad (5)$$

and e is the total specific energy in Eq. (4), given by

$$e = (1/2)u_i \cdot u_i + u_e \quad (6)$$

In the preceding set of equations, we neglected the Soret and Dufour effects, radiative heat losses, and body forces. Chemical kinetic source terms and molecular transport properties are computed through an interface with the CHEMKIN set of subroutines. We model species transport using unity-Lewis-number (UL) and mixture-averaged (MA) [31] models. In the UL model, all the species are assumed to have the same mass diffusivity, equal to the thermal diffusivity of the mixture. In the MA model, Fickian-type diffusion is assumed, similar to the UL model, but differential diffusion is accounted for by computing the mixture-averaged diffusivity D_{km} of each species k as

$$D_{km} = \frac{1 - Y_k}{\sum_{j \neq i} \frac{X_j}{D_{ji}}} \quad (7)$$

where D_{ji} is the binary diffusion coefficient for species j diffusing into species i, X_j is the mole fraction of species j, and N is the total number of species.

Spatial discretization is achieved through a compact sixth-order finite difference scheme [32], whereas a compact-storage fourth-order Runge–Kutta scheme [33] is employed for time integration. Nonreflective outflow boundary conditions are prescribed at all the boundaries using the Navier–Stokes characteristic boundary conditions (NSCBC) method of Poinsot and Lele [34]. Here, the NSCBC method has been extended to account for multicomponent gaseous mixtures in the estimation of the characteristic wave amplitudes [30]. The code is written in FORTRAN 90 and parallelized using MPI. Further details on the implementation can be found in [30].

B. Chemical Kinetic Mechanism

We choose *n*-heptane as the surrogate for practical fuels and model its oxidation chemistry with a skeletal mechanism comprising 34 species among 56 reaction steps developed by Peters et al. [25]. The 56-step mechanism describes first- and second-stage ignition. In [25], it was shown that this mechanism predicts autoignition delay times in *n*-heptane/air mixtures with adequate accuracy for pressures up to 42 bar. We assessed the accuracy of the mechanism to predict nonpremixed flame structure, extinction, and partially premixed flame structure through comparisons with available experimental data in *n*-heptane flames at 1 bar. These results are discussed next.

For nonpremixed flame structure and extinction, we consider the experimental data reported by Seiser et al. [35] for counterflow gaseous *n*-heptane/air flames. Seiser et al. report profiles of temperatures and major species mole fractions for a counterflow flame with 15% molar *n*-heptane and 85% molar N_2 at 338 K on one side ($x = 0$) and with air at 298 K on the other side ($x = 1$). The fuel- and oxidizer-side velocities are 0.342 and 0.375 m/s, respectively. The OPPDIFF code [36] is employed to compute the steady-state structure of the nonpremixed flame.

Figure 1a compares the computed temperature profile using the 56-step mechanism with the measured data. Note that about 250 grid points were employed to obtain a grid-independent solution. Figure 1a shows that the mechanism predicts the peak temperature and its location within 5%, even though some discrepancies are observed on the fuel side. Figure 1b compares the computed profiles of CO_2 and CO mole fractions with the measured data. The agreement of the peak values is within 8% for CO_2 and within 15% for CO. In addition, we compared profiles of other major species such as H_2O and H_2 (and C-1 and C-3 hydrocarbons such as CH_4 and C_3H_6) and found that the values predicted by the mechanism were within 25% of the measured values.

To compute extinction strain rates, the fuel- and oxidizer-side velocities were gradually varied; starting from a steady-state burning solution in OPPDIFF until a turning point leading to a nonburning solution was observed. Figure 1c compares the computed and measured extinction strain rates as a function of O_2 mass fraction on the air side. The mechanism captures the qualitative behavior well and the predicted values lie within 20% of the measurements.

To assess the applicability of the 56-step mechanism to predict a partially premixed flame structure, we consider the recent experimental data reported by Berta et al. [37]. In these experiments, temperatures and species concentrations in counterflow flames established with a partially premixed *n*-heptane/air mixture at a given equivalence ratio Φ and 400 K at one end ($x = 0$) and with air at 298 K on the other end ($x = 1.5$) were measured. We compared the measured data with computed data for cases with $\Phi = \infty$ (nonpremixed), 4, and 10 at a global strain rate a_g of 100/s. For brevity, we present the temperature and H_2 and H_2O mole fraction comparisons in Figs. 2a and 2b, respectively, for the $\Phi = 10$ case. We observe that the agreement is reasonably good with respect to peak locations and magnitudes. These comparisons lend credence to the applicability of the 56-step mechanism to predict nonpremixed and partially premixed flame structures and extinction.

Note, however, that in the present work, we are employing the mechanism at a relatively high pressure of 40 bar. To the best of our knowledge, there is no experimental data in the literature on *n*-heptane flame structure and extinction under high pressures. This leads to a certain degree of uncertainty with respect to chemical kinetics in this work, and hence we will defer from drawing specific conclusions about the reaction pathways and chemical species governing reignition. Nevertheless, as shown in previous experimental and numerical studies on flame–vortex interactions [26,38], the interaction outcomes are predominantly governed by nondimensional numbers such as the Damköhler number and the Reynolds number. Hence, it is expected that the regimes observed in this work, such as reignition and pocket formation, will be observed even with a different kinetic model if the controlling nondimensional numbers are the same. It is therefore useful to interpret the 56-step *n*-heptane mechanism as one with a set of chemical time scales (Damköhler numbers).

C. Simulation Conditions and Parameters

The computational domain is 2-D, measuring 2.5×2.5 mm. The numerical grid is uniform with 350×350 grid points, which results in a resolution of about 7.1 μm. Note that this resolution is significantly higher than that employed in previous studies of hydrocarbon flames (40–50 μm) [23,27] in order to resolve the thin reaction zones at the high pressures simulated here. A mass diffusion layer is formed between pure gaseous *n*-heptane and diluted air ($15\%O_2 + 85\%N_2$ molar), given by the following hyperbolic-tangent profile:

$$f = \left(\frac{f_1 + f_2}{2}\right) + \left(\frac{f_2 - f_1}{2}\right)\tanh\left(\frac{Y - Y_c}{\delta}\right) \quad (8)$$

where f is the mass fraction of a given species at a particular location, and f_1 and f_2 are the mass fractions of the species on the fuel and air sides, respectively; Y and Y_c are the Y coordinates of a given location and the center, respectively; and δ is the thickness of the hyperbolic-tangent profile. In this work, we are interested in simulating conditions representative of the near field of high-Reynolds-number jets, such as those in diesel chambers. RANS computations of gaseous *n*-heptane jets under diesel-like conditions [8] show that the conditional mean scalar dissipation rate at $x/d = 30$ in a 420,000

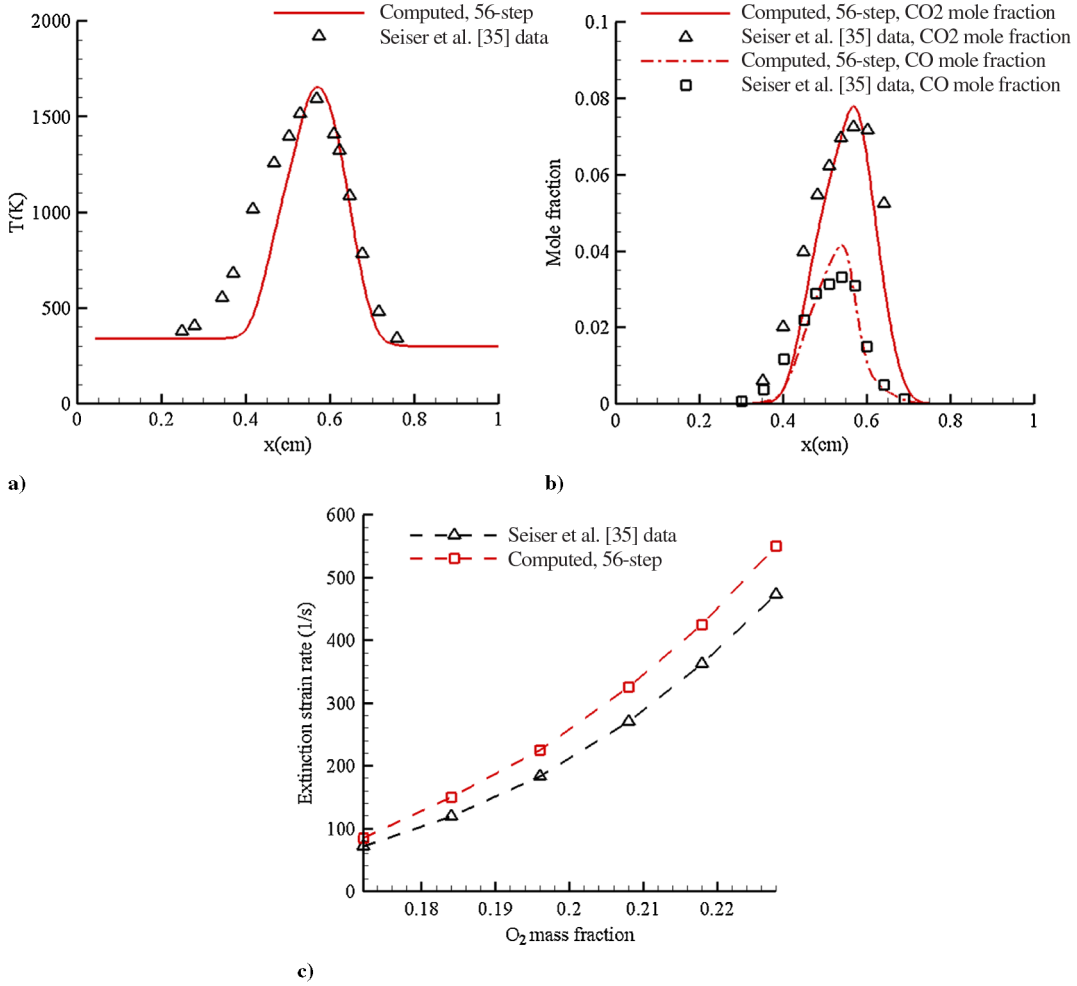

Fig. 1 Nonpremixed flame structure and extinction computed with the 56-step mechanism compared with the measured data of Seiser et al. [35]: a) temperature, b) mole fractions of CO_2 and CO, and c) extinction strain rates as a function of O_2 mass fraction.

Reynolds number jet is about 21/s. Hence, we choose $\delta = 100\ \mu$m, which gives rise to an initial stoichiometric scalar dissipation rate $\chi_{st,i}$ of 21/s. To ascertain how close the initial flame is to extinction, it is useful to define a nondimensional parameter R [20] as

$$R = \frac{\chi_e}{\chi_{st,i}} \tag{9}$$

For the range of simulated conditions, R is about 6.1. The relatively small value of R (less than 10) employed here simulates the presence of highly strained flamelets in the near field of high-Reynolds-number jets. Note that changing the value of δ would change the relative size of the vortex with respect to the flame and, in turn, curvature effects. We will explore the effects due to curvature on

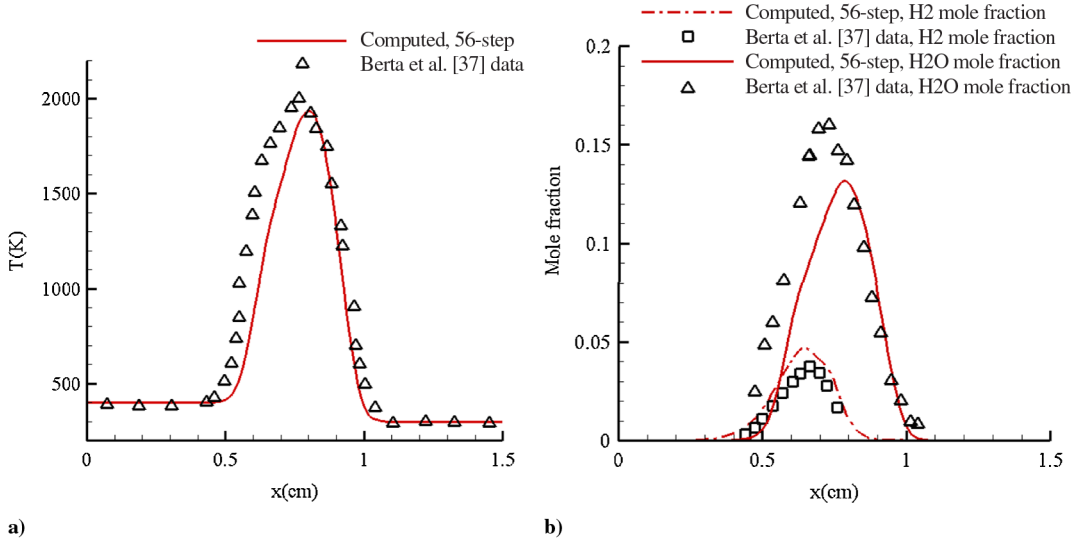

Fig. 2 Comparison of computed and measured data of Berta et al. [37] for a n-heptane counterflow partially premixed flame with $\Phi = 10, a_g = 100$/s: a) temperature and b) H_2 and H_2O mole fractions.

reignition. In addition, the value of R would change through $\chi_{st,i}$, and hence the robustness of the initial flame. In this work, we limit our analysis to changes in the vortex characteristics. It would be useful to investigate variations of R (i.e., flame characteristics) in future investigations.

Note that the selected grid resolves δ by about 14 grid points. It is typical in reacting DNS to resolve reaction zones by about 10 grid points [39]. Based on previous studies of reacting mixing layers [29] with the present numerical code, the selected resolution is adequate to explore physical mechanisms. However, we performed a simulation with 625×625 grid points, which gives a uniform resolution of 4 μm, in order to assess whether our conclusions regarding the mechanisms for extinction/reignition are affected by numerical resolution. Important variables such as the temperature, major species mass fractions, and diffusive/convective fluxes of mixture enthalpy computed with the finer resolution were compared with the 350×350 grid. The same mechanisms (discussed in Sec. IV.A), such as partially premixed combustion and curvature effects, were observed during extinction/reignition with both resolutions, though there were some minor differences with respect to magnitudes and the spatial spread of the extinguishing/reigniting regions. Because our focus is on the mechanisms for extinction/reignition, the selected resolution of 7.1 μm is adequate for the simulated conditions. The fuel-side temperature is 450 K and the air-side temperature is 1000 K. The simulated pressure is 40 bar. These conditions are typical of practical combustion chambers (e.g., diesel chambers).

Note that we employ the ideal-gas equation of state (EOS) in the present work. The simulated pressure of 40 bar and the fuel-side temperature of 450 K are not far from the critical pressure (27.4 bar) and critical temperature (540.3 K) of n-heptane. It is therefore possible that the EOS may influence the conclusions. To assess the influence of the EOS, the mixture density was recomputed as a postprocessing step from the Redlich–Kwong EOS [40] and compared with that using the ideal-gas EOS. This comparison showed negligible differences in the flame zone, where N_2 is the major constituent, up to a mixture fraction of 0.8. Recall that the flame zone is where our interest lies. The fuel-side density, beyond a mixture fraction of 0.8, from the Redlich–Kwong EOS was as much as 52% higher than that from the ideal-gas EOS. This higher density may affect the residence times for the flame–vortex interaction somewhat. If we employ jet-scaling laws to the air-side vortex jet, the vortex (convection) velocity scale would have to be increased by about 20% to achieve comparable residence times. This 20% increase in the velocity scale may have an influence on the time scales for extinction/reignition, but it will not influence the underlying physical mechanisms. Hence, using the ideal-gas EOS in this work is a reasonable simplification.

A 1-D flamelet library [41] is employed to obtain initial conditions for the diffusion flame. Figure 3a shows the mixture fraction Z, computed from elemental mass fractions using Bilger's [42] definition. Figure 3b shows a magnified view of the initial temperature contours with the velocity vectors superimposed, showing a counter-rotating vortex pair on the oxidizer side. To mimic the vortex numerically, each vortex of the counter-rotating vortex pair is superimposed on the initial flowfield on the air side as an Oseen–Hammel vortex [13] according to the expression

$$u_\theta = \frac{\Gamma}{2\pi r}\left(1 - \exp\left(-\frac{r^2}{\sigma^2}\right)\right) \tag{10}$$

where u_θ is the circumferential velocity, Γ is the circulation, r is the radial distance from the vortex center, and σ is the core radius, which is sufficiently small compared with the initial vortex diameter d_v to begin with ($\sigma < 0.3d_v$) and thereafter increases with time due to viscous action. In Eq. (10), Γ is an input parameter that characterizes the velocity scale u_v of the vortex pair and the Reynolds number of the vortex. This technique of impulsively starting the vortex has been employed in previous flame–vortex-interaction studies (see, for instance, Cuenot and Poinsot [38], and Renard et al. [13]. As discussed by Vera and Linan [43], the velocity scale u_v of the vortex pair is the self-propagation velocity, given by

$$u_v = \frac{\Gamma}{2\pi d_v} \tag{11}$$

All the vortices considered in this study are initialized at a distance of about 2.5δ from the peak temperature location in the flame. Though this location lies in the thermal layer, we found that because of the relatively high vortex Reynolds numbers employed (175–900), thermal expansion does not significantly attenuate the vortex strength before interaction with the flame.

Note that the 2-D assumption is an important simplification in this work because realistic 3-D effects such as vortex-stretching on the flame dynamics are ignored. In the present case, the 2-D assumption is justified for the following reason. The early analytical work of Karagozian and Marble [44] on diffusion-flame sheets subject to vortex interaction shows that the only effect of vortex-stretching is to modify the distribution of the rolled-up combustion products in the vortex. The authors found the enhancement in the reactant consumption rate to be identical between a 2-D planar vortex and a 3-D vortex stretched along its axis. Indeed, the 2-D assumption is very typical of flame–vortex-interaction studies, and [24,27,45] are recent examples of 2-D flame–vortex-interaction studies that have provided useful insights. Hence, given the modest improvement in the physics, the significant computational overhead associated with 3-D

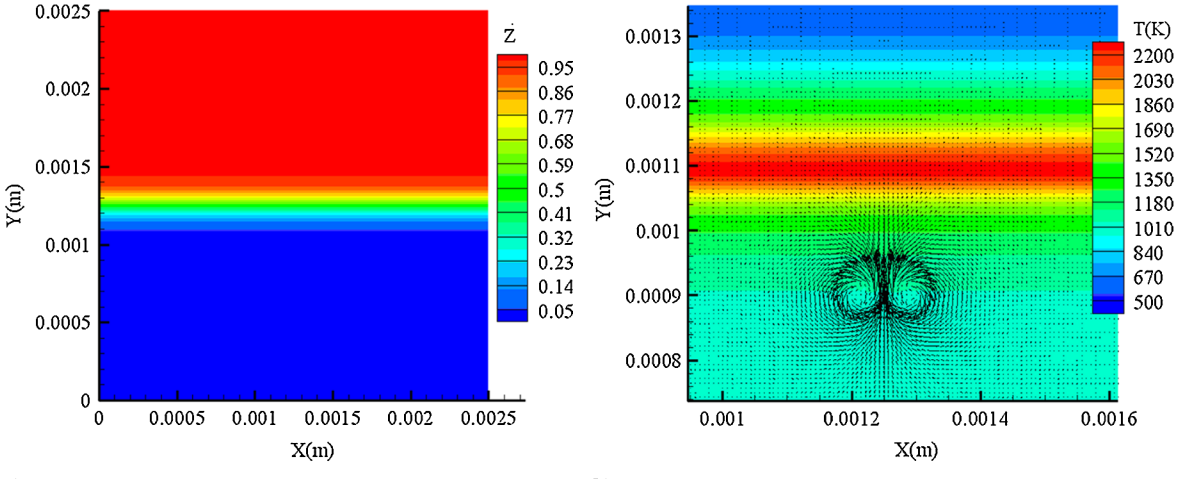

Fig. 3 Initial conditions: a) mixture fraction contours and b) temperature contours and velocity vectors.

simulations is not justified. In addition, note that previous studies in the literature [20,46] have reported annular extinction events that occur only in an axisymmetric configuration and hence cannot be captured by the Cartesian formulation employed here. However, the results of Hermanns et al. [20] show that annular extinction events are probable only for robust flames (i.e., flames initially far from extinction). Hermanns et al. [20] show that annular extinction events occur for relatively robust flames with $R = 14.5$ and 25, but axial extinction is favored for relatively weak flames with $R = 5.5$. As mentioned before, R is about 6.1 in the present case and hence it is reasonable to expect that axial extinction is more probable than annular extinction. Hence, the 2-D Cartesian formulation employed here is adequate to resolve the relevant physics for the range of conditions simulated.

It is useful to introduce nondimensional numbers based on the vortex and flame scales that characterize the flame–vortex interaction. Consider the following three nondimensional numbers:

1. Length-Scale Ratio l_r

Based on the initial vortex diameter d_v (core-to-core distance) and the initial diffusion-layer thickness δ, we can define a length-scale ratio l_r as

$$l_r = \frac{d_v}{\delta} \tag{12}$$

where l_r is a measure of the vortex-induced curvature effects and varies in the range of 0.7–1.8 in this work. Because $\delta = 100$ μm, the simulated vortices have initial diameters in the range of 70–180 μm. Note that the integral length scales in a diesel jet may be of the order of the orifice diameter, which typically lies in the range of 100–400 μm. Hence, the simulated vortices in the present study are comparable to the integral scales in a diesel jet.

2. Time-Scale Ratio τ_r

A characteristic time scale for the vortex may be defined as

$$\tau_v = \frac{d_v}{u_v} \tag{13}$$

Note that this definition results in a time scale twice that defined by Vera and Linan [43] in which $(d_v/2)$ was used as the length scale. Based on a representative chemical time scale τ_c for the flame, we can introduce a time-scale ratio τ_r as

$$\tau_r = \frac{\tau_c}{\tau_v} \tag{14}$$

where τ_c can be estimated from the steady extinction scalar dissipation rate $\chi_e(s^{-1})$ as [39]

$$\tau_c = \chi_e^{-1} \tag{15}$$

For the conditions simulated, χ_e is estimated to be about 130 s^{-1} using a 1-D flamelet library with the 56-step mechanism. Note that τ_r may be interpreted as an inverse of a Damköhler number and is a measure of the vortex-induced unsteadiness on the flame response. In the present work, τ_r varies in the range of 640–1650. In other words, strong unsteady effects are expected in the flame response. Large values of τ_r emulate interactions of strong vortices with flamelets that are likely to occur in the near field of high-Reynolds-number jets. Note that while changing τ_r, u_v varies in the range of 7.5–15 m/s. The turbulent velocity scale in the near field $(x/d < 30)$ of a diesel jet may be of the order of the injection velocity, which typically lies in the range of 200–600 m/s. Assuming fully developed turbulence intensity (~10%), the velocity scale may be of the order of 20–60 m/s in a diesel jet. Hence, the simulated range of u_v is comparable to velocity scales in the near field of diesel jet flames.

Table 1 Simulated cases

Case	l_r	τ_r	Re	Transport
Baseline	0.7	1650	350	MA
A	0.7	825	175	MA
B	1.8	640	900	MA
C	0.7	1650	350	UL

3. Vortex Reynolds Number

Based on d_v and u_v, we can define a vortex Reynolds number Re as

$$Re = \frac{u_v \cdot d_v}{\nu} = \frac{\Gamma}{2\pi\nu} \tag{16}$$

using Eq. (11) for u_v. Note that the preceding definition of Re differs from that of Vera and Linan [43] and Glezer [47] ($Re = \Gamma/\nu$) by a factor of 2π, but is physically consistent in that the Reynolds number is directly related to Γ. In the present work, the Reynolds number of the simulated vortices varies in the range of 175–900 and was chosen to represent turbulent integral length-scale Reynolds numbers in the near field $(x/d < 30)$ of jets with inlet Reynolds numbers in the range of 50,000–400,000 and global mixing rates $(U_{\text{inj}}/d_{\text{noz}})$ in the range of $25,000$–$200,000$ s^{-1}. Extinction/reignition phenomena would be prevalent in the near field of such jets. Note that in terms of previous definitions [42,47], the Reynolds number range is 1099–5652, which lies within the laminar/turbulent transition Reynolds number of 10^4 suggested by Glezer [47] and Dimotakis [48]. Hence, the simulated vortices have relatively high Reynolds numbers, but lie within the laminar regime. Note that because the Reynolds number depends on both u_v and d_v, it represents the combined effects of unsteadiness and curvature.

Table 1 shows the simulation parameters for the different cases investigated. Note from Table 1 that cases A and B represent changes in the velocity scale and the length scale of the vortex relative to the baseline case, respectively. Case C is compared with the baseline case to assess the influence of the transport formulation on the flame–vortex interaction. The computations were performed in parallel with 64 processors on the NCSA Xeon Supercluster. The CPU time varied between 5–8 days, depending on the strength of the vortex simulated.

IV. Results and Discussion

We will first explore the mechanisms leading to reignition for the baseline case with $l_r = 0.7$, $\tau_r = 1650$, and $Re = 350$ and then investigate effects due to unsteadiness, curvature, and transport formulation on the rate of reignition and product formation. We will close this section with a discussion of the implications of the observed flame–vortex-interaction outcomes for turbulent combustion modeling.

A. Flame Structure and Mechanism for Reignition

Figure 4 shows the sequence of events that occur after local extinction during the flame–vortex interaction for the baseline case. In Fig. 4, the physical time elapsed is nondimensionalized by the initial turnover time scale of the vortex t_{eddy} (d_v/u_v) to give t^*. Representative values of the mixture fraction Z are also indicated on the figure, with $Z = 0.05$ being the stoichiometric Z in the present case. We observe two distinct edge flames bordering the quenched region along the vertical centerline. Note that following extinction, the extinguished regions are considerably diluted by the oxidizer, indicated by the relatively small values ($Z \sim 0.01$) values of Z. As time progresses, the edge flames are rolled up by the vortex-induced flow. In addition to roll-up, lateral interactions occur between the edge flames, leading to their merger. We also observe that secondary local extinction events occur in the reigniting region due to high rates of partial premixing that form fuel-rich mixtures. The merged flame eventually evolves into a reconnected diffusion flame.

It is seen that the OH mass fraction tracks the temperature. Furthermore, a fuel-rich pocket detached from the reconnected flame is formed that propagates on the fuel side. Figure 4 also shows the

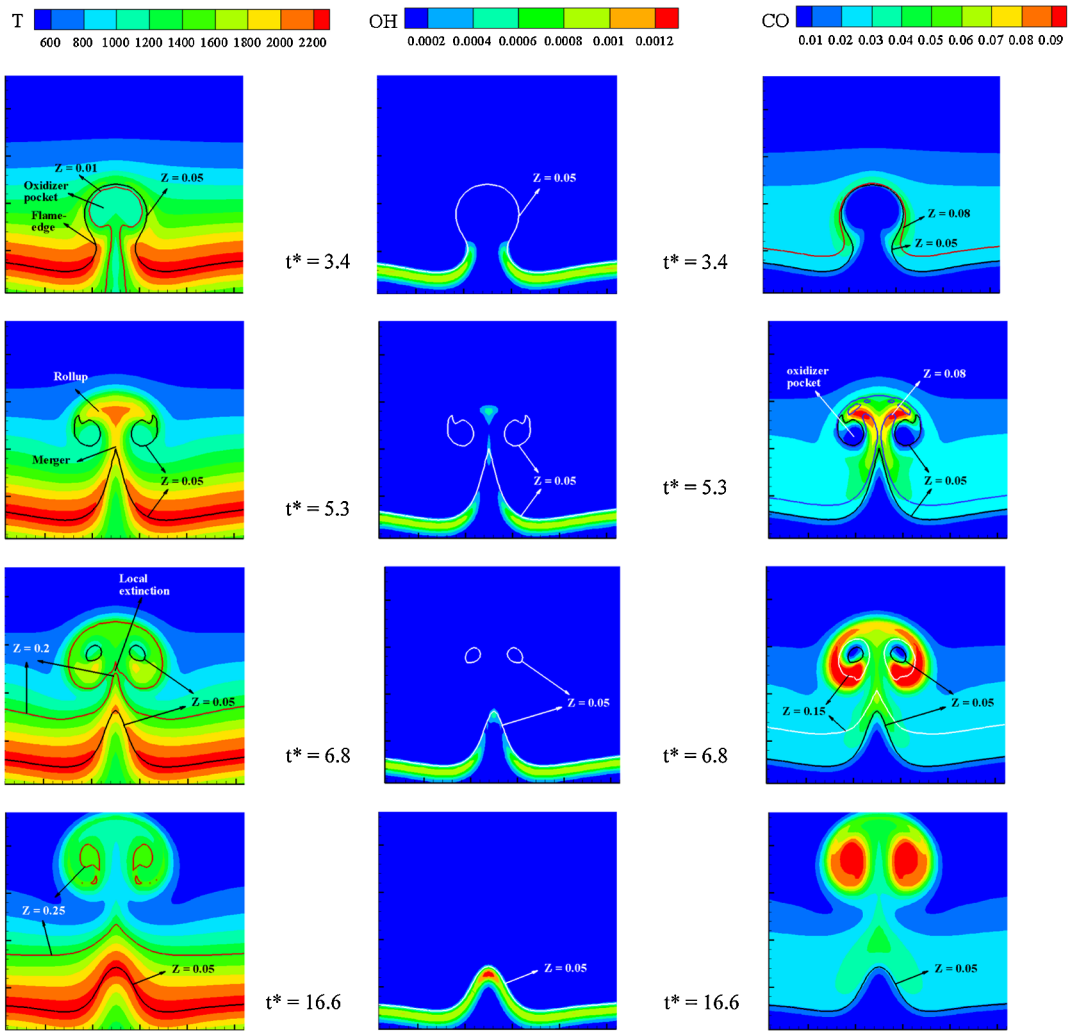

Fig. 4 Sequence of events during the flame–vortex interaction for the baseline case in terms of the contours of temperature (K) (left), OH mass fraction (middle), and CO mass fraction (right).

time evolution of the mass fraction of CO, which is an important byproduct in hydrocarbon combustion. As expected, CO essentially forms in rich mixtures. The vortex-induced stretch leads to concentrations of CO higher than in the original diffusion flame. It is interesting that the detached partially premixed pocket acts as a major source of CO formation. Though not shown here, H_2 is also formed primarily in the vortical pocket. This could have implications for pollutants such as soot. Hence, even though promoting reignition is desirable from a flame-stability consideration, the present results indicate that reignited flamelets may be surrounded by fuel-rich pockets in which pollutants can form. We will explore this tradeoff in greater detail later, when considering effects due to unsteadiness and curvature. Now, we will investigate the nature of flow–chemistry interactions occurring during reignition.

To quantify the mixing rate, it is customary to introduce the instantaneous scalar dissipation rate χ, defined as

$$\chi = 2D_Z(\nabla Z)^2 \tag{17}$$

where $D_z = \lambda/(\rho c_p)$ is the mixture fraction diffusivity, assuming a unity Lewis number for the mixture fraction [27]. In addition, we introduce a nondimensional scalar dissipation rate χ_r, given by

$$\chi_r = \frac{\chi_{\mathrm{st}}}{\chi_e} \tag{18}$$

where χ_{st} is the instantaneous scalar dissipation rate at stoichiometric Z. Values of χ_r less than unity represent burning flames. The recent flame–vortex studies of Oh et al. [27] indicate that unsteady effects can lead to extinction scalar dissipation rates greater than the steady value χ_e. Hence, values of χ_r greater than unity may either represent burning flames (due to unsteadiness) or extinguished flames. In other words, the greater the value of χ_r compared with unity, the greater the unsteady effect due to the vortex.

To investigate the mechanisms for reignition, let us consider DELHX, which is the lateral diffusion term for mixture enthalpy h. Figures 5a–5d show the time evolution of DELHX. DELHX is computed as

$$\mathrm{DELHX} = \frac{\partial}{\partial X}\left(\frac{\lambda}{c_p}\frac{\partial h}{\partial X}\right) \tag{19}$$

In addition, the locations of the flame edges can be obtained as the intersections of the isocontours of a reactive scalar and the stoichiometric mixture fraction ($Z \sim 0.05$) [10]. Here, in Figs. 5a–5d, we choose the $T = 2000\ K$ isocontour along with the $Z = 0.05$ isocontour to identify the edge flames. Representative values of χ_r at two locations are also indicated in the figures: one is the edge location and the other is the maximum value along the stretched $Z = 0.05$ isocontour.

We observe from Fig. 5a that soon after local extinction ($t^* = 3.4$), the edge flames border the quenched region and transfer heat through the DELHX term. Note that the relatively large values of χ_r ($\sim$15) shown in Fig. 5a indicate that the unsteady extinction limit is significantly higher than the steady value χ_e. This finding differs from the experimental observations of Santoro et al. [19], in which the unsteady limits were reported to be only about 30% higher than the steady limit. An important difference between our conditions and those investigated by Santoro et al. is the relative magnitude of the

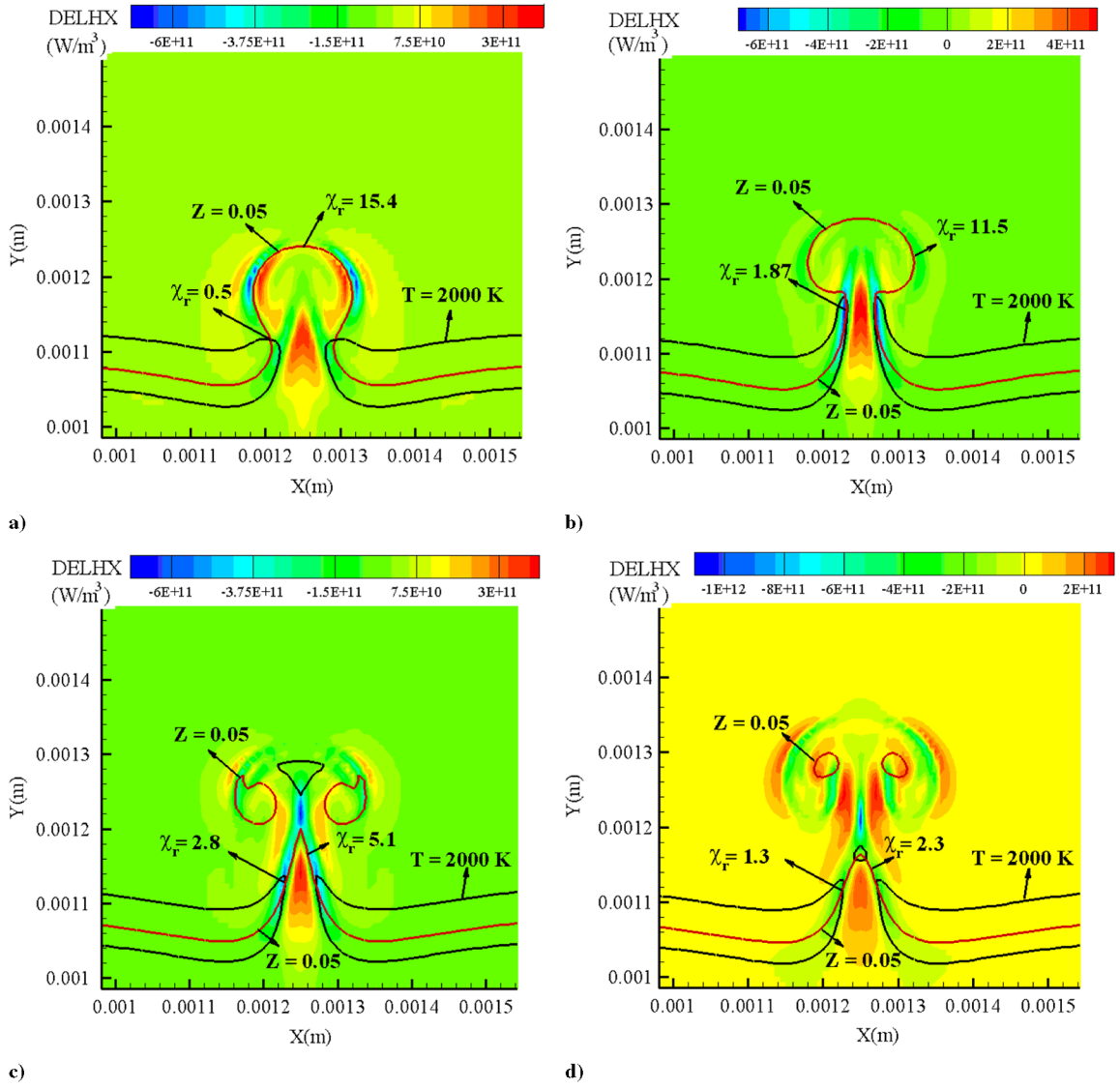

Fig. 5 Evolution of the lateral heat diffusion term (W/m^3) during reignition at a) $t^* = 3.4$, b) $t^* = 4.2$, c) $t^* = 5.3$, and d) $t^* = 6.8$.

characteristic chemical time scale τ_c with respect to the vortex time scale τ_v. Although τ_c was shorter than τ_v in the experiments of Santoro et al., rendering the inner reactive-diffusive layer quasi-steady, τ_c is much longer than τ_v (see the values of τ_r in Table 1) in this work, rendering the reactive-diffusive layer unsteady. Hence, the unsteady flame responds with a significant delay to the imposed strain, resulting in unsteady extinction limits much higher than the steady value. This conclusion is also qualitatively consistent with the recent flame–vortex studies of Oh et al. [27] that report unsteady limits as much as 4 times the steady value, due to vortex time scales being shorter than chemical time scales.

Note that the value of χ_r at the flame edge is low enough ($\chi_r \sim 0.5$) to favor its propagation into the extinguished region, whereas the maximum value of χ_r occurs at the vortex tip. As time progresses, the edges are rolled up and brought into proximity in the wake of the vortex-induced flow, enhancing the magnitude of DELHX in the reigniting region. However, observe from Figs. 5b and 5c that the $Z = 0.05$ isocontour is significantly strained, indicated by values of χ_{st} that are 2–3 times χ_e at the edge locations. This prevents further propagation and causes the edge flames to recede away due to negative propagation in the presence of high scalar dissipation rates [18]. Also note that in Fig. 5c, DELHX contributes to heat loss from the reignited fuel-rich regions to the colder fuel-lean regions around the vortical pocket, which leads to the secondary local extinction events discussed before in Fig. 4. Subsequently, we observe from Fig. 5d that by $t^* = 6.8$, values of χ_r at the edge locations have relaxed to values close to unity, creating conditions favorable for propagation and eventual reconnection of the diffusion flame. Hence, consistent with the previous DNS study of Pantano [10] and the counterflow experiments of Santoro et al. [18], the edge-flame dynamics are strongly influenced by excursions of χ_{st} above and below χ_e However, note that due to significant delay in the flame response to the imposed scalar dissipation (unsteady effects), the edge flames withstand χ_{st} values well above χ_e without extinction. This underscores the need to account for unsteady effects in edge-flame propagation models, rather than to use χ_e to distinguish positive and negative propagation characteristics of edge flames regardless of the flow, as in recent theoretical works [20,43].

To estimate the importance of DELHX relative to other heat fluxes, consider Figs. 6a and 6b, which compare the convective and diffusive terms for h along the vertical centerline at $t^* = 3.4$ and 5.3, respectively. Note that the vertical centerline is a symmetry axis and represents a stretched flamelet ($0 < Z < 1$) that undergoes extinction/reignition due to interaction with the vortex. Hence, this diagnostic axis is useful to explore the validity of the 1-D flamelet assumption during extinction/reignition. The temperature is also shown on the right-hand-side axis. In the figures, CNVHY and DELHY are the convective and diffusive terms, respectively, for mixture enthalpy. These are computed as

$$\text{CNVHY} = \rho v \frac{\partial h}{\partial y} \tag{20}$$

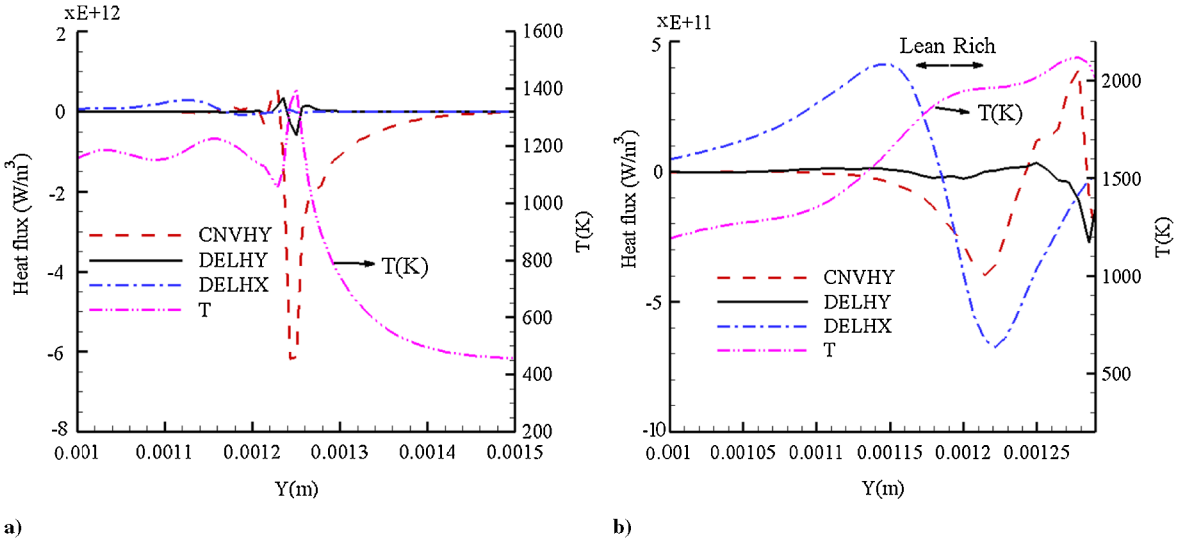

Fig. 6 Comparison of convective and diffusive heat fluxes (W/m^3) at a) $t^* = 3.4$ and b) $t^* = 5.3$ during the flame–vortex interaction. The temperature (K) is shown on the right axis.

$$\text{DELHY} = \frac{\partial}{\partial y}\left(\frac{\lambda}{c_p}\frac{\partial h}{\partial y}\right) \tag{21}$$

Note that the convective term in the X direction is zero because the vertical centerline is a symmetry axis.

Figure 6a shows that close to local extinction, the dominant mode of heat loss is the convective term in the flame normal (Y) direction, CNVHY, followed by the normal diffusion term DELHY, but the lateral (curvature) term DELHX is negligible. This indicates a 1-D flamelet-type behavior, which was observed in the flame response during the extinction phase. However, in contrast, Fig. 6b shows that during reignition at $t^* = 5.3$, DELHX plays a dominant role, leading to heat addition (from the adjoining edge flames) in the fuel-lean regions and heat loss (to the colder vortical pocket) in the fuel-rich regions. Hence, in violation of the flamelet assumption, curvature (2-D) effects leading to lateral interactions between quenched and neighboring burning regions become significant during reignition. Note that the DNS study of Sripakagorn et al. [15] indicates that reignition could also occur through flamelet autoignition, which would be governed by normal diffusion. However, in the present case, owing to the relatively high Reynolds number of the vortex, the vortex-induced partial premixing causes reignition to occur through lateral interactions before flamelet autoignition can occur.

We can conclude from the results discussed so far that under the relatively high vortex Reynolds numbers simulated here, mutual interactions between edge flames manifesting as lateral heat diffusion are responsible for the reignition of the extinguished regions. Note that this scenario differs from the experimental observations of Santoro et al. [19], in which the relatively weaker vortices dissipate significantly following extinction and reignition occurs solely by the propagation of the edge flames along the stoichiometric contour. In the present case, the vortices survive through the entire flame–vortex-interaction period and have a dominating influence on the edge-flame dynamics. However, the present reignition scenario shows good qualitative agreement with the edge-flame propagation and engulfment scenarios reported by Sripakagorn et al. [15] in reacting isotropic turbulence, in which the contribution of the lateral heat diffusion term was found to be important. Their study showed that the engulfment and edge-flame propagation scenarios are favored when there are significant excursions of χ above χ_e during local extinction. This is consistent with the observations in the present work, because local extinction is associated with large excursions of χ above χ_e (i.e., $\chi_r \gg 1$).

In the context of modeling, it is useful to characterize the mode of combustion (diffusion/premixed) during reignition. To do this, we introduce the cross-scalar dissipation rate L, defined as [49]

$$L = 2D_Z \nabla Y_F \cdot \nabla Y_O \tag{22}$$

where Y_F and Y_O represent the mass fractions of the fuel and oxygen, respectively. Also called the flame index [15], L may be used to identify regions with premixed and diffusion modes of combustion. From Eq. (22), it is clear that L is positive for the premixed mode, whereas it is negative for the diffusion mode.

Figures 7a–7c show the variation of L as a function of the Y coordinate along the vertical centerline at $t^* = 3.4$, 5.3, and 6.8, respectively. The mass fractions of fuel (Y_F) and oxygen (Y_O), and the mixture fraction (Z) are shown on the right-hand-side axis. In addition, the Z_{st} value ($\sim$0.05) is indicated by a dashed line in the figures. At $t^* = 6.4$, soon after extinction and at the onset of reignition, we observe a strong diffusive mode of combustion, indicated by the relatively large negative values of L. As time progresses, at $t^* = 5.3$ and 6.8, we observe from Figs. 7b and 7c that both positive and negative values of L occur in the reigniting region, indicating a mixed or partially premixed mode of combustion. Note that along the vertical centerline (symmetry axis) shown in the figures, only the Y derivatives are nonzero in the ∇ operator. It may be deduced from Figs. 7a–7c that the positive and negative signs of L are in fact consistent with the signs of ∇Y_F and ∇Y_O. For instance, consider the variation of L in Fig. 7b. We observe that $L < 0$ in the region $0.00115 < Y < 0.0012$ because Y_F increases (i.e., $\nabla Y_F > 0$) and Y_O decreases ($\nabla Y_O < 0$), whereas $L > 0$ in the region $0.0012 < Y < 0.00125$ because both Y_F and Y_O decrease. Moreover, as seen from Figs. 7b and 7c, there exist premixed regions ($L > 0$) that are flammable (Z–Z_{st}), into which the neighboring edge flames can propagate to promote reignition. Hence, these observations further confirm that transient reignition evolves through a partially premixed flame structure and purely diffusion-flamelet libraries are not applicable.

Having explored the basic mechanisms and flow–chemistry interactions during reignition, we will now focus on the separate effects due to unsteadiness and curvature on reignition and product formation.

B. Influence of Unsteadiness

To explore the influence of unsteadiness on reignition, case A (see Table 1) at a lower value of τ_r equal to 825 was simulated in addition to the baseline case, while maintaining l_r constant at 0.7. In other words, the velocity scale u_v of the vortex for case A is half of that for the baseline case. Hence, case A corresponds to a lower vortex Reynolds number Re of 175.

Figures 8a and 8b show the contours of the lateral diffusion term DELHX along with the isocontours of $T = 2000$ K and $Z = 0.05$, at $t^* = 5.3$ and $t^* = 6.8$, respectively, for case A. Values of χ_r at the

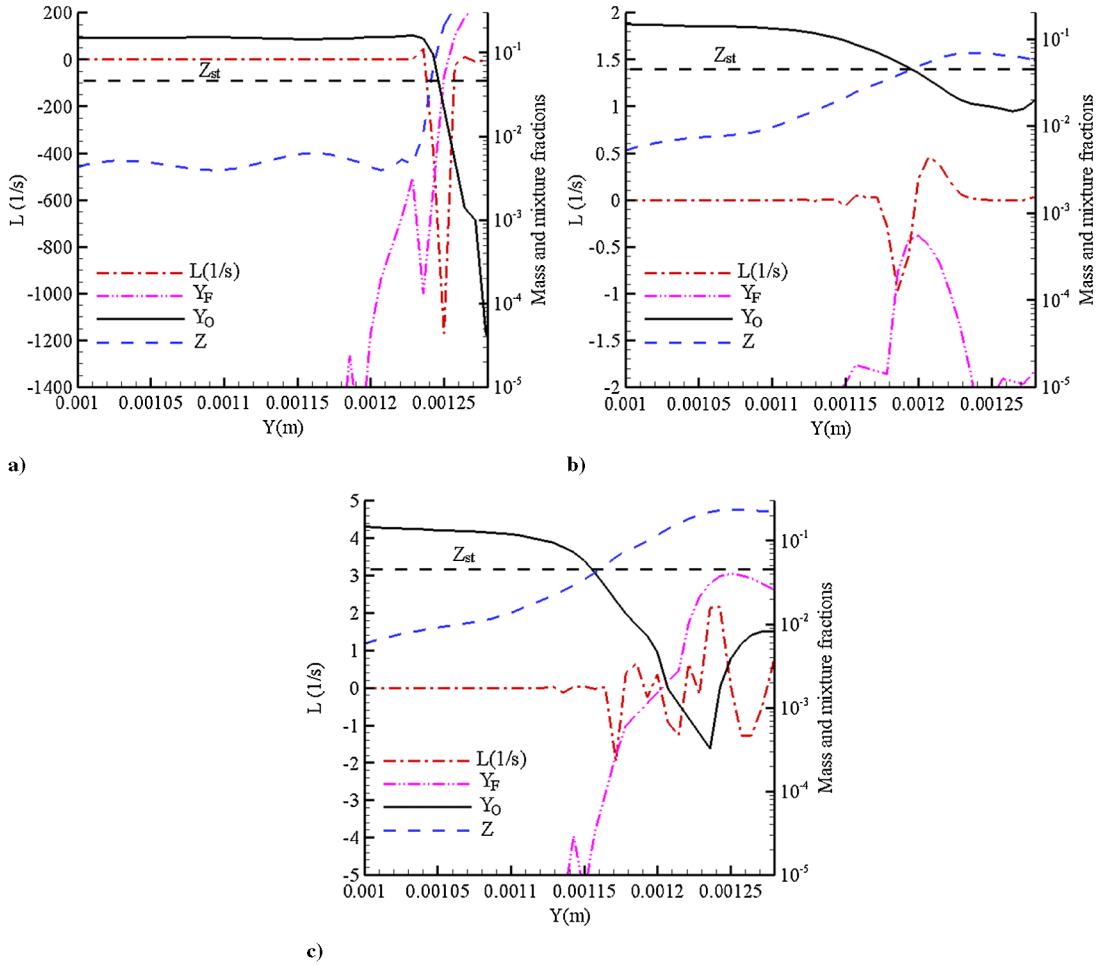

Fig. 7 Cross-scalar dissipation rate L (1/s), and the mass fractions of fuel (Y_F), oxygen (Y_O), and the mixture fraction (Z) along the vertical centerline at a) $t^* = 3.4$, b) $t^* = 5.3$, and c) $t^* = 6.8$.

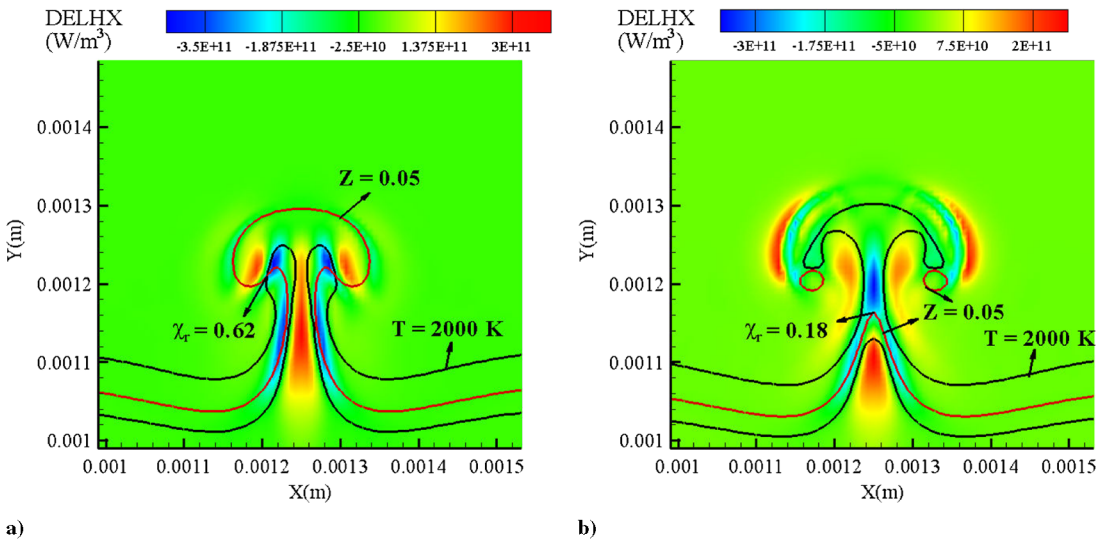

Fig. 8 Contours of DELHX (W/m^3) for case A at a) $t^* = 5.3$ and b) $t^* = 6.8$.

flame-edge location are also indicated in the figures. Comparing Figs. 8a and 8b with Figs. 5c and 5d for the baseline case, we observe much lower values of χ_r, which allow the edge flames to be significantly rolled up into the cores of the vortex. However, as seen from Fig. 8a, roll-up causes the edge flames to recede away from the extinguished regions and delays the reconnection of the diffusion flame. Note that the edge flames merge through lateral interactions by $t^* = 6.8$, which is twice as long in physical time as that of the baseline case.

To quantify the increase in flame roll-up from the baseline case ($Re = 350$) to case A ($Re = 175$), consider Fig. 9, which shows the total burned area and the total premixed burned area as a function of time t^* for both cases. The burned area is computed as the area above a temperature of 1500 K, and the premixed area is the fraction of this

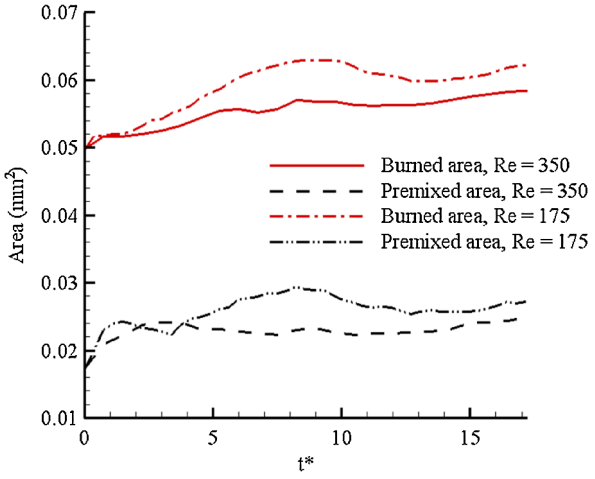

Fig. 9 Total burned and premixed areas (mm^2) as a function of t^*.

area with a positive value of the flame index L. The choice of the temperature cutoff is arbitrary, but is useful to compare trends between the two cases. We observe from Fig. 9 that as a result of greater flame roll-up, the slower vortex ($Re = 175$) leads to a larger burned area. Moreover, due to sufficient residence times for the flame–vortex interaction, a larger fraction of the burned area is premixed in the case of $Re = 175$ relative to $Re = 350$. Hence, although a decrease in the unsteadiness (vortex velocity) increases the extent of flame roll-up and burned fractions, the rate of reignition through mutual interactions between edge flames decreases.

We will now compare the cases with $Re = 350$ and 175 with respect to the formation of the major products of combustion (i.e., CO_2, H_2O, CO, and H_2). Figures 10a–10d show the total partial density (ρY_k) of CO_2, H_2O, CO, and H_2 in the computational domain as a function of t^* for the two cases. We observe from Figs. 10a and 10b that the interaction with the slower vortex yields slightly higher amounts of CO_2 and H_2O (about 6%), which is consistent with the greater flame roll-up and increased burned area (see Fig. 9). Moreover, we notice from Fig. 10c that with respect to the total amount of CO (per unit volume), the differences between the two cases are even smaller. Figure 10d shows that the yield of H_2 is rather insignificant in comparison to the other products, but the slower vortex results in somewhat less H_2.

To clarify these trends, let us consider the time instant $t^* = 12$ and investigate the product distributions for the baseline case and case A. Figures 11a–11d show the contours of the mass fraction of CO_2 and CO for the baseline case and case A, respectively. Note from the figures that even though the nondimensionalization of t by t_{eddy} (d_v/u_v) to give t^* accounts for the initial differences in the propagation velocities of the vortex pairs between the two cases, the faster vortex (baseline case) has reached a somewhat higher Y position in comparison to case A. This could be due to greater viscous dissipation and attenuation of the vortex strength for case A, which is indicated by the CO_2 and CO distributions in the vortex cores being more diffused in this case. Also note from Figs. 11a and 11b that the reconnected flame is thicker (in terms of CO_2 mass fraction) for

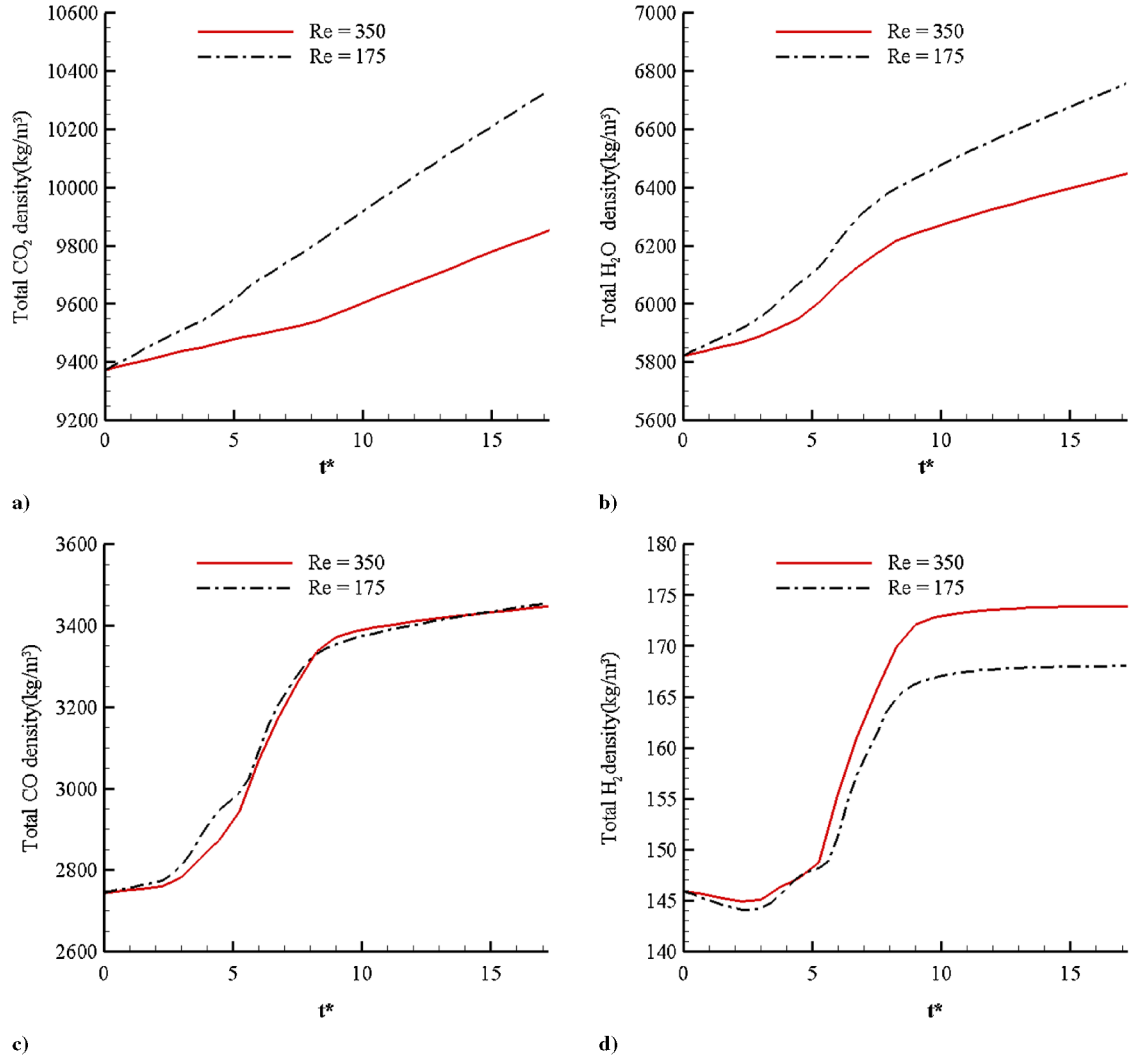

Fig. 10 Total density (kg/m^3) as a function of t^* for the cases with $Re = 350$ (baseline) and 175 (case A): a) CO_2, b) H_2O, c) CO, and d) H_2.

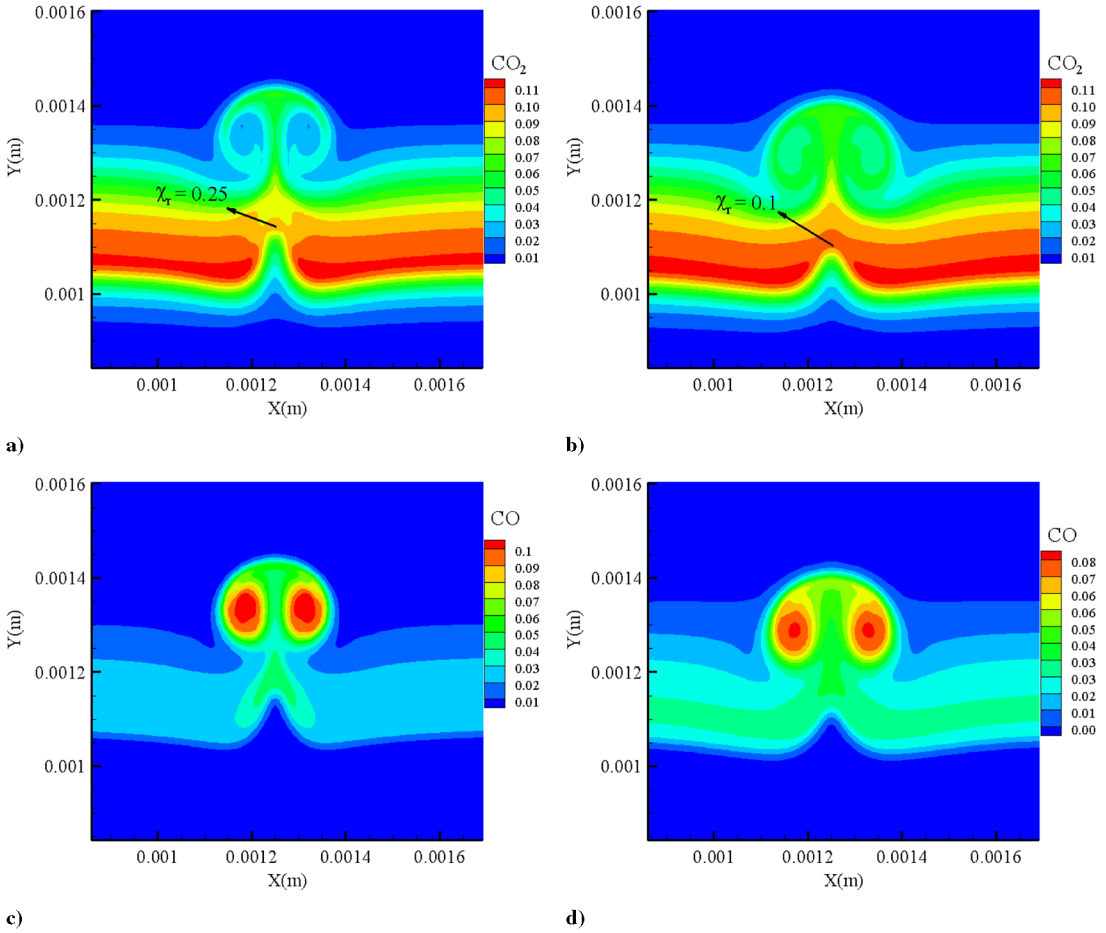

Fig. 11 Contours of the mass fraction of CO_2 and CO at $t^* = 12$: a) CO_2, baseline case, b) CO_2, case A, c) CO, baseline case, and d) CO, case A.

case A, owing to lower scalar dissipation rates. Hence, a thicker reconnected flame in the case of the $Re = 175$ vortex leads to higher total concentrations of CO_2, as shown in Fig. 10a. In addition, Figs. 11a–11d show that the spatial locations for predominant CO_2 and CO formation differ significantly. Although CO_2 forms predominantly in the reconnected flame, CO mostly forms in the fuel-rich pocket.

Figures 12a and 12b show the CO mass fraction and the scalar dissipation rate χ as a function of the X coordinate along the horizontal line passing through the vortex centers for the baseline case ($Re = 350$) and case A ($Re = 175$) at $t^* = 12$. Observe from Fig. 12b that the χ values are much lower in the $Re = 175$ case and the shifts in the peak locations between the two cases occur due to the radial expansion of the $Re = 175$ vortex as a result of viscous dissipation. The greater dissipation of the $Re = 175$ vortex leads to lower peak values and more diffuse profiles for CO, as shown in Fig. 12a. However, note that Fig. 10c shows the total yield of CO as a function of time, which is similar to the integrated area under the curves in Fig. 12a at each time instant and are hence predicted to be about the same.

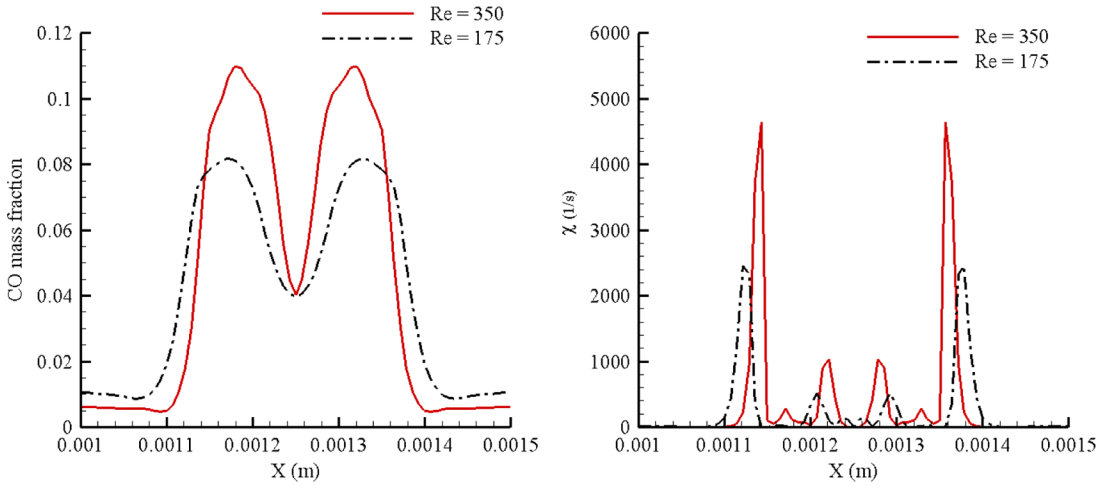

Fig. 12 Comparison of the baseline case ($Re = 350$) and case A ($Re = 175$) along the horizontal line passing through the vortex centers at $t^* = 12$: a) CO mass fraction and b) χ.

C. Influence of Curvature

Now we will investigate the effects due to the variation of the vortex length scale d_v, which is a measure of the vortex-induced curvature, on the reignition and product formation characteristics. Below, we present results from case B (see Table 1) with $l_r = 1.8$, $\tau_r = 640$, and $Re = 900$. For this case, d_v of the vortex is about 2.5 times that for the baseline case, whereas u_v remains constant. Hence, t_{eddy} for case B is about 2.5 times that for the baseline case, and we will nondimensionalize the time elapsed using t_{eddy} as before.

Figures 13a–13c show the contours of DELHX for case B at different values of t^*. As before, isocontours of $T = 2000$ K and $Z = 0.05$, along with representative values of χ_r, are indicated in the figures. We observe a rather large extinction hole (compare with Fig. 4, top left) bordered by the flame edges in Fig. 13a, comparable to the length scale of the vortex in this case. This implies that in comparison to the baseline case, there are significantly more diluted fractions ($Z < 0.01$) following extinction that need to premix and form flammable fractions for reignition to occur. Figure 13b shows that the vortex enhances the burning area through a complete roll-up of the edge flames into the cores of the vortex. Note that flame roll-up has an effect similar to negative propagation in that it causes the edge flames to recede away from the extinguished regions. As in the case of the smaller vortex (baseline case), DELHX contributes toward heat loss from the reignited rich fractions in the region $0.0012 \text{ m} < Y < 0.0014 \text{ m}$ along the vertical centerline, leading to local extinction and secondary edge flames. The flame begins to reconnect by $t^* = 5.3$ as χ_r values at the edge locations relax below unity (Fig. 13c). Note that because t_{eddy} for case B is about 2.5 times that for the baseline case, the reconnection process occurs over a longer time period in actual physical time, implying that the rate of reignition decreases as the vortex size increases. Hence, larger extinguished fractions and enhanced flame roll-up are two factors that weaken the mutual interactions between the edge flames and lead to a lower rate of reignition with a larger vortex.

Figure 14 shows the time evolution of the total burned and premixed burned areas for the baseline case ($Re = 350$) and case B ($Re = 900$). We observe a significant increase in the burning area (defined here as the area above 1500 K) with the $Re = 900$ vortex as opposed to the $Re = 350$ vortex. The premixed burning area (i.e., the area above 1500 K and $L > 0$) remains greater for the $Re = 900$ vortex, but we observe rapid variations in the magnitudes with time. This suggests that the mode of combustion rapidly shifts between premixed and diffusion modes locally in the case of the larger vortex.

To explore the influence of curvature on the product formation, consider Figs. 15a–15c. Figure 15a compares the total mass of CO_2 per unit volume between the two cases. We observe trends consistent with the increase in burning area in that the $Re = 900$ vortex yields higher amounts (about 26%) of CO_2. Similar trends were observed in the case of H_2O. The total amount of CO also shows a significant increase (Fig. 15b), and it is interesting to note from Fig. 15c that the ratio of CO mass to CO_2 mass increases from about 30 to 50% as the Reynolds number increases from 350 to 900. In addition, Fig. 15c shows that the relative amount of H_2 with respect to H_2O is insignificant for both cases.

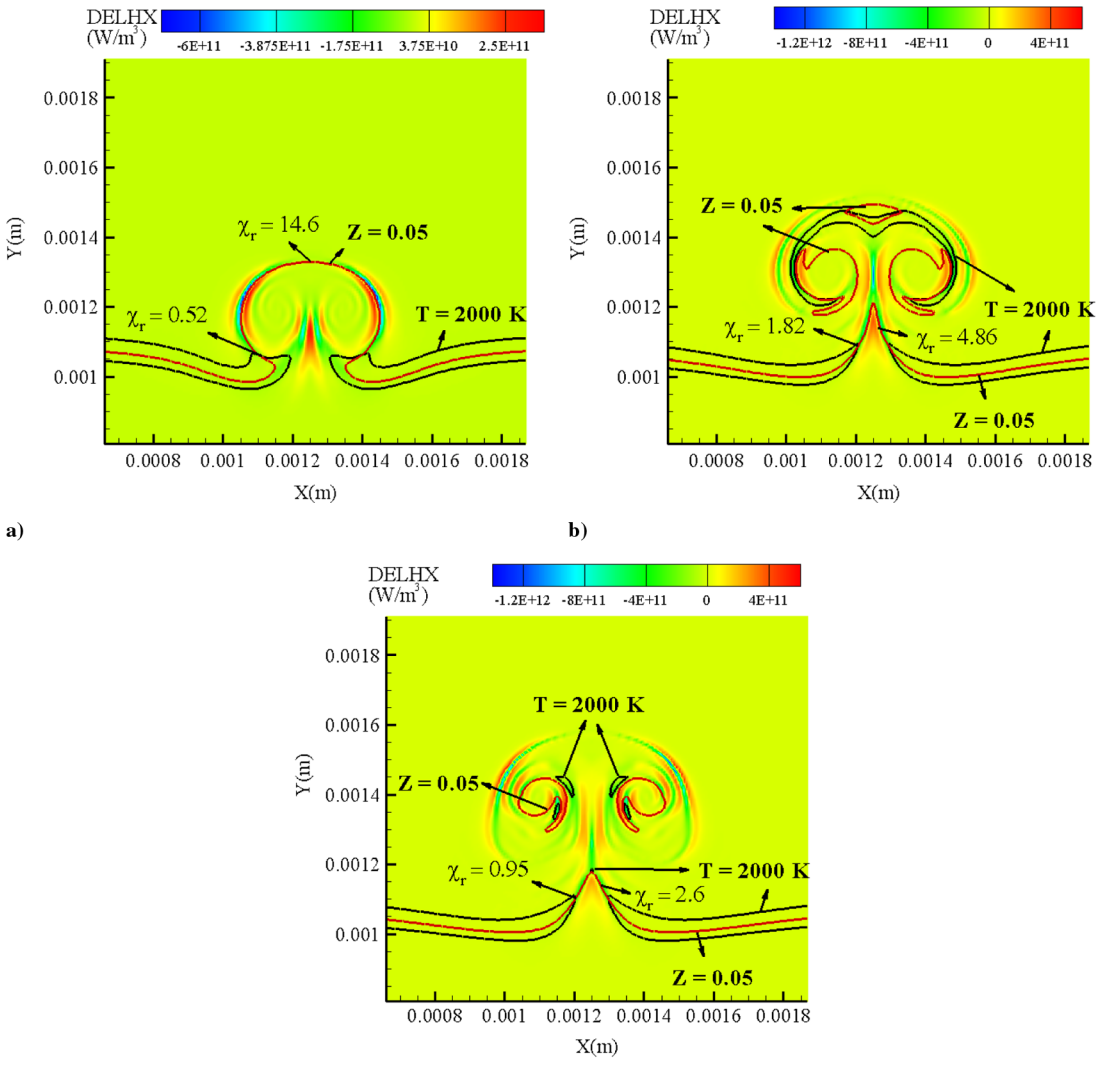

Fig. 13 Contours of DELHX (W/m^3) for case B at a) $t^* = 1.8$, b) $t^* = 4.2$, and c) $t^* = 5.3$.

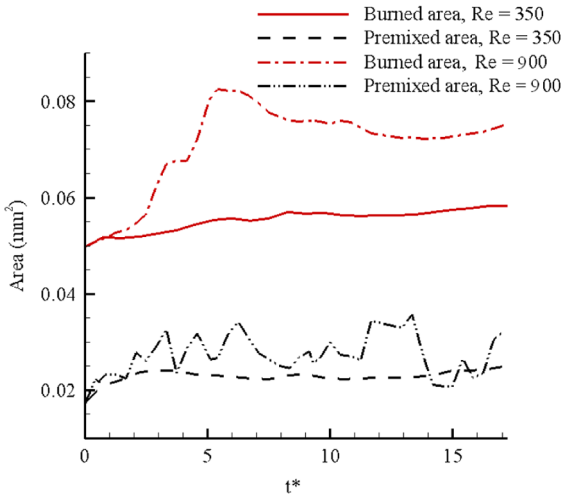

Fig. 14 Total burned and premixed areas (mm^2) as a function of t^*.

The preceding observed trends can be understood through an examination of the instantaneous distributions of Z and species concentrations (say, at $t^* = 17$). Figures 16a–16d show the contours of CO_2 and CO for the baseline case ($Re = 350$), and case B ($Re = 900$), respectively. Isocontours of $Z = 0.05$, 0.15, and 0.25 are also overlaid on the figures. Note that $t^* = 17$ actually represents a longer physical time in the case of $Re = 900$ (because t_{eddy} increases), and because both cases have the same initial velocity scale u_v, the $Re = 900$ vortex has propagated much further on the fuel side. We observe a much larger vortical pocket (about 2.5 times) on the fuel side in the $Re = 900$ case, which is a predominant source for CO formation. In addition, we also notice somewhat higher concentrations of CO in the reconnected flame in the case of $Re = 900$, possibly due to higher scalar dissipation rates. This leads to higher total concentrations of CO, as shown in Fig. 15b, even though the peak magnitudes are higher in the $Re = 350$ case at $t^* = 17$. Moreover, higher amounts of CO_2 are also formed in the pocket when $Re = 900$ relative to $Re = 350$, as seen from Figs. 16a and 16b. This is attributed to leaner mixtures in the cores of the vortices in the $Re = 900$ case, as indicated by the Z isocontours. Essentially, higher rates of partial premixing due to the vortex-induced curvature lead to richer fractions ($Z > 0.15$) in the case of $Re = 350$, thereby decreasing the amount of CO_2 formed in the pocket. Hence, similar to CO, the total amounts of CO_2 also increase as the vortex size increases.

From the discussion on the effects of unsteadiness and curvature, it can be concluded that it is beneficial to have high rates (higher velocity scales) of fine-scale (smaller length scales) mixing with respect to flame stability (rate of reignition). Moreover, the present results show that the global mixing rate induced by the vortex ((u_v/d_v)) is a direct measure of the rate of reignition. For instance,

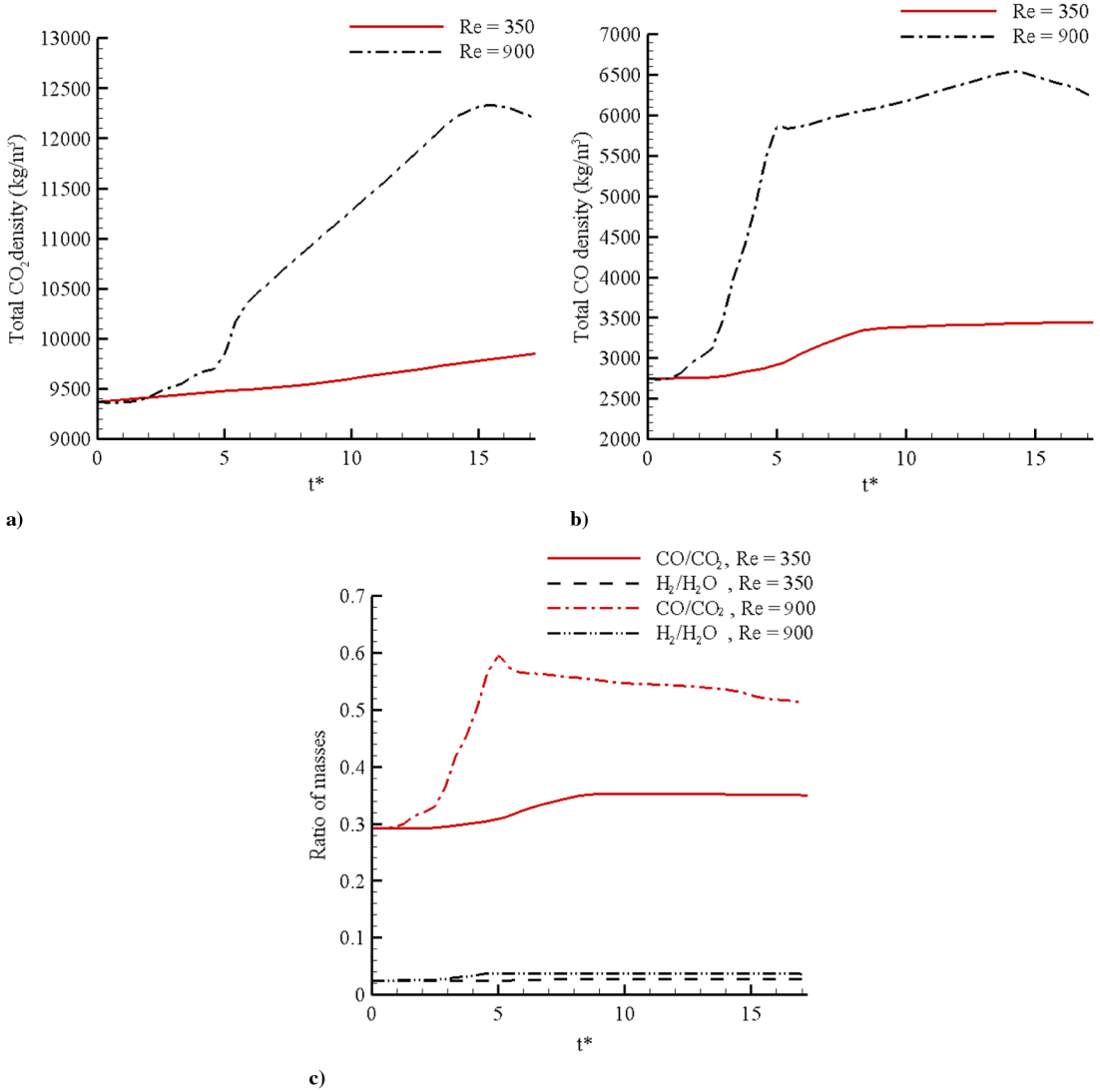

Fig. 15 Comparison of the cases with $Re = 350$ (baseline) and $Re = 900$ (case B) with respect to a) total CO_2 density (kg/m^3), b) total CO density (kg/m^3), and c) ratio of CO mass to CO_2 mass and H_2 mass to H_2O mass.

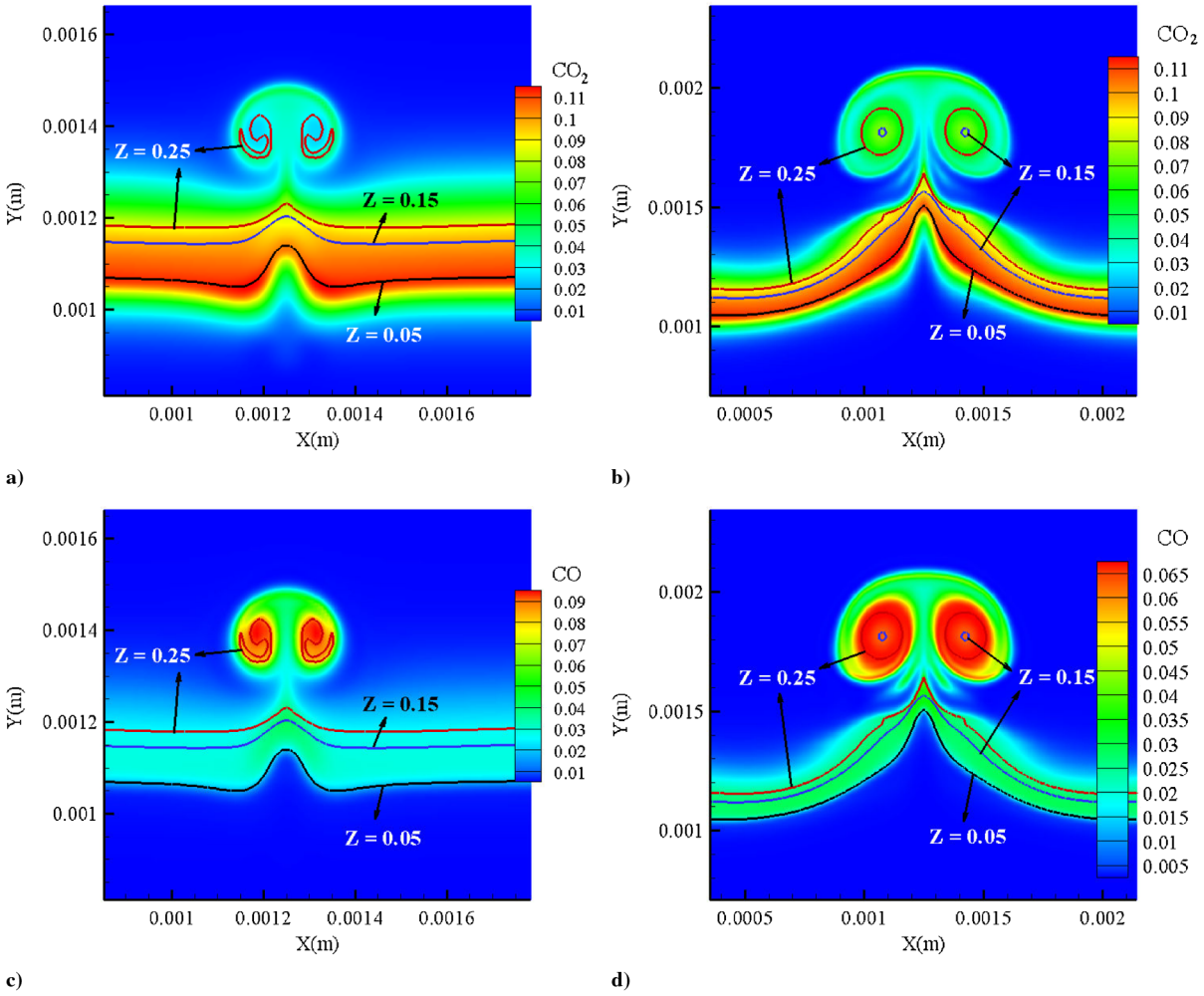

Fig. 16 Comparison of the baseline case ($Re = 350$) and case B ($Re = 900$) at $t^* = 17$, with respect to contours of a) CO_2 mass fraction, baseline case, b) CO_2 mass fraction, case B, c) CO mass fraction, baseline case, and d) CO mass fraction, case B.

the rate of reignition decreases for both cases A and B relative to the baseline case, due to a decrease in u_v/d_v. On the other hand, larger length scales lead to higher rates of formation and higher yields of combustion products. However, higher velocity scales lead to higher rates of formation of the products, but the overall yield may decrease, due to reduced residence times for the flame–vortex interaction.

D. Influence of Transport Formulation

It is useful to investigate the influence of the transport formulation on the flame structure during reignition. Note that the simplified UL model is widely employed in flamelet modeling of turbulent nonpremixed combustion [50]. Case C is identical to the baseline case, with the difference that it assumes UL for transport. These two cases are now compared.

Consider Figs. 17a–17c, which compare the MA and the UL models with respect to temperature, OH, and H_2 mass fractions, respectively, at different times during the flame–vortex interaction. We observe negligible differences between the models with respect to temperature in Fig. 17a. Small differences were also observed with respect to the mass fractions of the major species (CO_2, CO, and H_2O). Figure 17b shows some differences between the MA and UL models with respect to OH mass fraction, but the differences are within 10%. However, with respect to the H_2 mass fraction, we observe significant differences between the models in Fig. 17c. For instance, at $t^* = 15$, the H_2 mass fraction profile is more diffuse with the MA model than with the UL model. The observed differences are expected because the Lewis number of H_2 is typically about 0.1 [51], which implies that the UL model underestimates the mass diffusivity by about an order of magnitude. Note that though the mass fraction of H_2 is much smaller than that of the major species such as CO_2, CO, and H_2O, these differences could have important implications for pollutants such as soot, which form through the hydrogen-addition/carbon-abstraction pathways [52].

To summarize, the present results indicate that for the conditions explored here, with respect to the temperature and major species concentrations, the UL model is a good approximation for transport. A likely reason is that in a higher-order hydrocarbon flame such as the present one, species with Lewis numbers very different from unity (such as H_2 and H) are in relatively small proportions and hence do not affect the overall characteristics of the flame. Previous flame–vortex-interaction studies [46] have shown differential diffusion effects to be important in H_2/air flames.

E. Implications for Turbulent Combustion Modeling

We will now discuss the implications of the results observed in this work to turbulent combustion modeling. For the relatively high vortex Reynolds numbers (175–900) employed here, mutual interactions between edge flames, formed during local extinction, play an important role during reignition. These interactions manifest as lateral species and heat diffusion from the rolled-up edge flames to the reigniting regions. In other words, vortex-induced curvature effects are critical during reignition. Moreover, examination of the flame-index L in the reigniting region showed that the combustion mode is mixed, involving both premixed and diffusion-mode burning.

In the context of modeling, it is useful to represent the simulated conditions on a turbulent combustion regime diagram, such as the

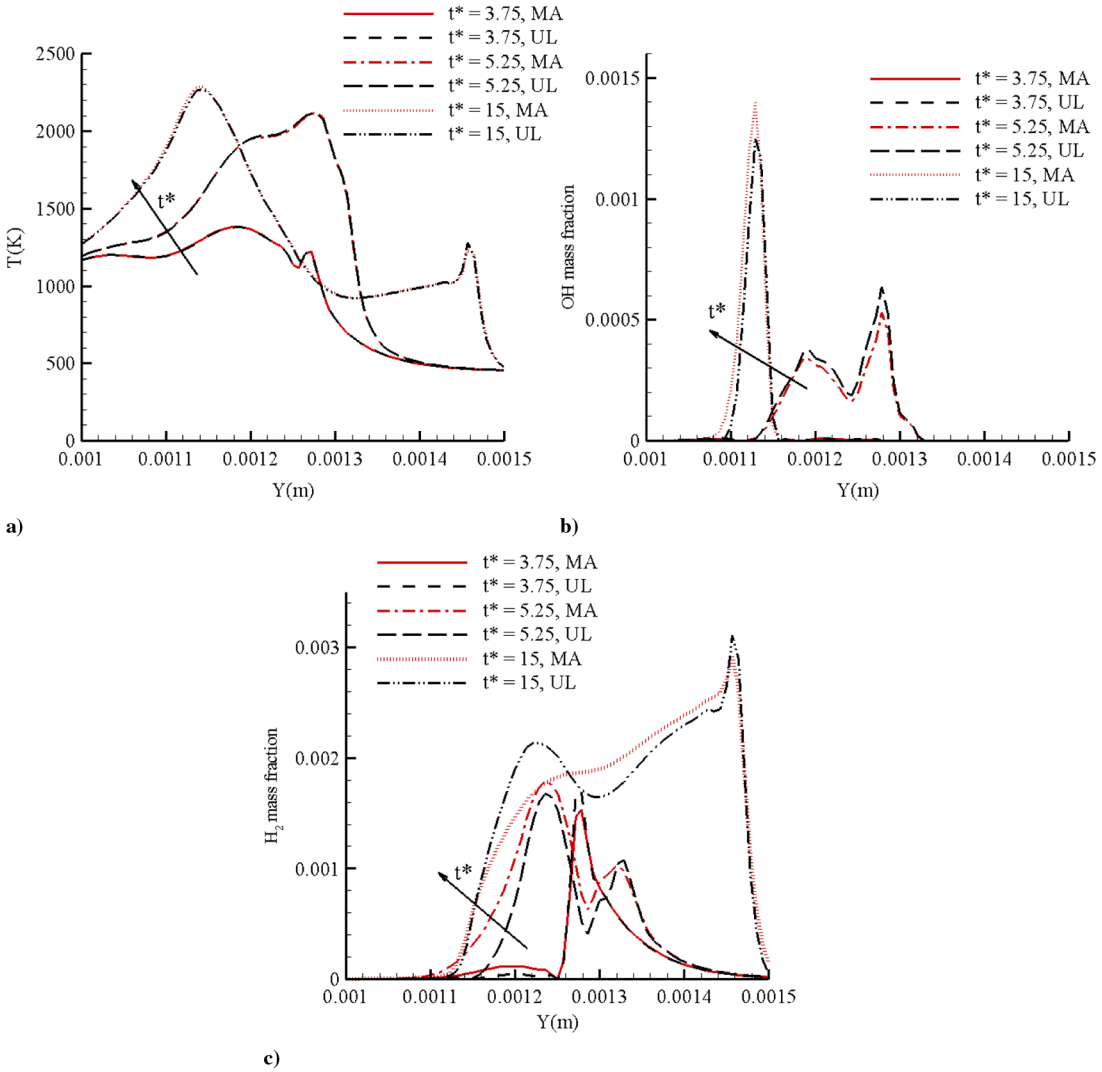

Fig. 17 Comparison of MA and UL models for the baseline case and case C with respect to the a) temperature (K), b) OH mass fraction, and c) H_2 mass fraction along the vertical centerline at different times.

one proposed by Peters [2]. This diagram is constructed with v'/s_L and l/l_F as axes, where l and l_F are the turbulent length scale and the laminar flame thickness, respectively, and v' and s_L are the turbulent velocity scale and laminar flame speed, respectively. In the present case, l and v' are given by d_v and u_v, respectively. Even though the regime diagram is valid for turbulent premixed combustion, it can be employed for nonpremixed flames by suitably defining flame length and velocity scales as [2]

$$\hat{l}_F = (\nu t_F)^{1/2} \tag{23}$$

$$\hat{s}_L = (\nu/t_F)^{1/2} \tag{24}$$

where t_F is the flame time of a stoichiometric premixed flame [2], given by

$$t_F = \frac{Z_{\text{st}}^2(1 - Z_{\text{st}})^2}{\chi_e} \tag{25}$$

In Eqs. (23) and (24), $\hat{l}_F$ is the characteristic flame length scale, and $\hat{s}_L$ is the flame velocity scale. Using Eqs. (23–25), we obtain $l/\hat{l}_F = 5.82$ and $v'/\hat{s}_L = 18.44$ for the baseline case; these lie within the thin (connected) reaction zone of the regime diagram. Note that this is consistent with the numerical results discussed so far, which predict a connected (reignited) flame following interaction with the vortex. Accurate modeling of local extinction/reignition is critical to predict the transient flame/vortex dynamics, and we discuss possible approaches next.

We may interpret the vertical centerline to be representative of a stretched flamelet ($Z = 0$ to 1 in mixture fraction space) that undergoes extinction and reignition as a result of the vortex interaction. It is then useful to construct a state diagram relating the temperature T and the scalar dissipation rate χ at a given value of Z (say, the stoichiometric value). For steady counterflow flames, this state diagram is the well-known S curve [12]. Figure 18 shows the T_{st}–χ_{st} state diagram for the baseline case constructed using the instantaneous data collected along the vertical centerline every 50 cycles up to about $t^* = 15$. Note that for the flame–vortex interaction under investigation, the characteristic chemical time scale is much longer than the vortex time scale ($\tau_r \gg 1$), rendering the reactive-diffusive layer unsteady and resulting in unsteady extinction limits that are much higher than the steady value. We observe three distinct parts of the T_{st}–χ_{st} curve, which are labeled as I, II, and III. The part of the curve represented by I is the burning branch. Part II of the curve represents the initial phase of reignition following extinction when dilution by the oxidizer pocket reduces χ significantly, and the adjoining rolled-up edge flames transfer heat, thereby promoting reignition. The later stage of reignition involving mutual interactions between edge flames and their merger is represented by part III of the curve. The turning point M shown in the curve marks the formation of a merged flame beyond which χ values decrease to values low enough to form the reconnected diffusion flame. Hence, the present results show that the simulated vortices break up the flame locally,

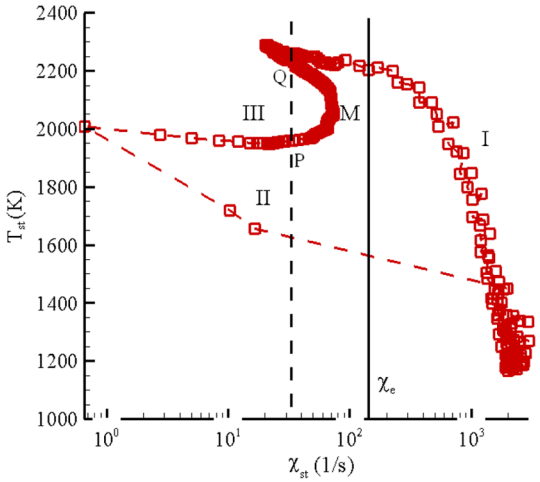

Fig. 18 T_{st}–χ_{st} state diagram for the baseline case.

causing extinction and a flame hole, which heals (or reignites) through a partially premixed flame structure. Next, we discuss one possible approach to account for partial premixing effects during reignition.

In the context of modeling, it is interesting to note that the commonly employed parameterization in flamelet models of the temperature in terms of Z and χ [i.e., $T = fn(Z, \chi)$, where fn is given by the solution of the flamelet equations [41]] is no longer unique to represent the states during reignition. For instance, along the dashed line shown in Fig. 18, a parameterization in terms of χ_{st} cannot distinguish between states P and Q. As discussed in the recent modeling work of Pitsch and Ihme [53], a reactive scalar such as the progress variable would be more useful. We can define a progress variable as the sum of the product mass fractions:

$$c = Y_{CO_2} + Y_{H_2O} + Y_{CO} + Y_{H_2} \tag{26}$$

Figure 19 shows the progress variable at the stoichiometric mixture fraction c_{st} as a function of χ_{st}. Being a reactive scalar, the dependence of c_{st} on χ_{st} shows similar trends to those of T_{st} on χ_{st}. In other words, lateral interactions between edge flames and the resulting partial premixing manifest as changes in c from unburned to burned values. Note that parameterization in terms of c alone does not provide a unique representation because, for instance, there are multiple states corresponding to $c_{st} = 0.17$ (see Fig. 19). However, these states can be distinguished with different values of χ_{st}. Hence, a flamelet library parameterized in terms of both χ and c [i.e., $T = fn(Z, \chi, c)$] can uniquely represent all the states encountered during extinction/reignition. Moreover, the unsteady flamelet

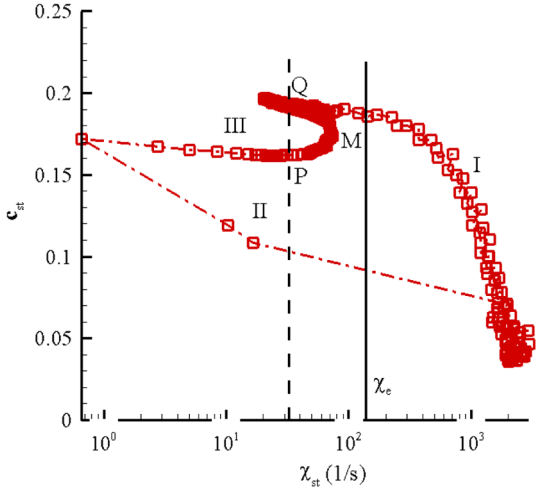

Fig. 19 The c_{st}–χ_{st} state diagram for the baseline case.

equations can be employed to obtain the range of values of c from burning to nonburning states for given values of χ. Note, however, that due to the high degree of unsteadiness and variability of χ in the present case, such a flamelet library has to span a wide range in terms of χ. Furthermore, this progress-variable-based flamelet model is conceptually similar to the two-dimensional unsteady flamelet model discussed in the recent work of Amantini et al. [54], in that the other dimension is represented by the progress variable.

V. Conclusions

A numerical investigation of reignition in nonpremixed n-heptane/air flames interacting with counter-rotating vortex pairs was carried out. The conditions employed were representative of those in practical combustors such as diesel chambers. The vortex Reynolds numbers simulated were in the range of 175–900 and were chosen to represent turbulent integral-scale Reynolds numbers in the near field of high-Reynolds-number jets. Oxidation of n-heptane was modeled with a 56-step skeletal mechanism. Species transport was modeled using the mixture-averaged approximation for multicomponent-species diffusion and the unity-Lewis-number model. We investigated the basic mechanisms leading to reignition and the effects due to unsteadiness (vortex velocity scale), curvature (vortex length scale), and transport formulation on the rate of reignition and product formation.

The results showed that for the range of conditions explored, reignition occurs through lateral (i.e., along the flame surface) interactions between edge flames created by local extinction. These interactions manifest as lateral species and heat diffusion from the rolled-up edge flames to the reigniting regions. In contrast to the classical flamelet assumption, the lateral diffusion term is of leading order and is dominant over diffusion and convection processes in the flame normal direction during reignition. Furthermore, investigation of a flame index that distinguishes regions with premixed and diffusion-mode burning in the reigniting region showed that the combustion is of mixed mode, confirming that purely diffusion-flamelet libraries are not applicable to predict the flame response during reignition. Following reconnection of the diffusion flame, a fuel-rich pocket was found to detach from the reconnected flame and propagate on the fuel side. This pocket is a predominant site for the formation of byproducts such as CO and H_2 and possibly pollutants such as soot.

Effects due to unsteadiness were studied by varying the vortex velocity scale. Decreasing the velocity scale was found to increase the extent of flame roll-up and burned fractions, but the rate of reignition decreased, owing to lower partial premixing rates. With respect to the formation of major products of combustion such as CO_2, CO, and H_2O, the rates of formation increased due to an increase in the velocity scale, but the overall yields of the products were not significantly different. Though the total amounts of CO_2 and H_2O showed a small increase, the total amount of CO formed was similar for a faster ($Re = 350$) and a slower ($Re = 175$) vortex. These trends were attributed to the greater viscous dissipation of the $Re = 175$ vortex and to the differences in the spatial locations for the formation of CO_2 and H_2O (reconnected flame) and CO (fuel-rich pocket).

Effects due to curvature were studied by varying the vortex length scale. Increasing the length scale by about 2.5 times led to a larger extinction hole that was significantly diluted by the oxidizer following local extinction. This increased the time scale for partial premixing and formation of flammable fractions in the reigniting region through mutual interactions between edge flames, thereby decreasing the rate of reignition. However, a significant increase in flame roll-up and burned fractions was observed in the case of the larger vortex. Furthermore, the total yield of combustion products such as CO_2 and CO was found to increase significantly. This was attributed to an increase in the size of the detached fuel-side pocket that forms after reconnection of the flame.

The choice of the transport formulation did not affect the preceding mechanisms for reignition. Comparison of the transient flame structure during reignition with UL and MA transport models

showed that the predicted flame temperatures and major species concentrations were similar between the two models. However, with respect to species such as H_2 and H, the predictions with the UL and MA models differed significantly, with the UL model resulting in higher peak magnitudes. These differences could have important implications for the predictions of the formation of pollutants such as soot.

Finally, we showed that the influence of the transient edge-flame dynamics on the reigniting flamelet can be represented on a $T-\chi$ state diagram. The states during the extinction phase resembled the upper branch of the S curve behavior of strained diffusion flames, but the unsteady flame was found to withstand χ values well above the extinction limit. Following extinction, reignition occurred through a series of states that included unstable behavior when both T and χ increase under the influence of the neighboring edge flames. The presence of the unstable behavior precludes the parameterization solely in terms of χ, and it was shown that parameterization in terms of a progress variable c in addition to χ would uniquely represent all the flame states during transient extinction/reignition.

We conclude by noting that although this work focuses on interactions of isolated vortices with nonpremixed flames, which is much more simplified than turbulence–flame interactions in the near field of a jet, they provide useful insights into possible mechanisms for reignition and product formation under high Reynolds numbers encountered in practical jets, and they provide directions for the development of improved models.

Acknowledgments

The authors gratefully acknowledge computing resources available under National Center for Supercomputing Applications (NCSA) grant number MCAO6N038. The numerical code employed in this work was developed by Vinicio Magi. The authors thank him for useful discussion during the course of this work.

References

[1] Bilger, R. W., "Turbulent Diffusion Flames," *Annual Review of Fluid Mechanics*, Vol. 21, 1989, pp. 101–135. doi:10.1146/annurev.fl.21.010189.000533

[2] Peters, N., *Turbulent Combustion*, Cambridge Univ. Press, Cambridge, England, U.K., Chaps. 3, 4, pp. 170–261, Jan. 2000.

[3] Poinsot, T., and Veynante, D., *Theoretical and Numerical Combustion*, R.T. Edwards, Philadelphia, 2005, Chap. 6, pp. 287–346.

[4] Siebers, D. L., and Higgins, B. S., "Flame Liftoff on Direct-Injection Diesel Sprays under Quiescent Conditions," Society of Automotive Engineers Paper 2001-01-0530, 2001.

[5] Siebers, D. L., Higgins, B. S., and Pickett, L. M., "Flame Liftoff on Direct-Injection Diesel Sprays: Oxygen Concentration Effects," Society of Automotive Engineers Paper 2002-01-0890, 2002.

[6] Venugopal, R., and Abraham, J., "A Review of Fundamental Studies Relevant to Flame Liftoff in Diesel Jets," *SAE 2007 Transactions: Journal of Engines*, Vol. 116, No. 3, 2007, pp. 32–151; also Society of Automotive Engineers Paper 2007-01-0134, 2007.

[7] Pickett, L. M., and Siebers, D. L., "Soot in Diesel Fuel Jets: Effects of Ambient Temperature, Ambient Density, and Injection Pressure," *Combustion and Flame*, Vol. 138, Nos. 1–2, 2004, pp. 114–135. doi:10.1016/j.combustflame.2004.04.006

[8] Venugopal, R., and Abraham, J., "A Numerical Investigation of Flame Liftoff in Diesel Jets," *Combustion Science and Technology*, Vol. 179, No. 12, 2007, pp. 2599–2618. doi:10.1080/00102200701487095

[9] Senecal, P. K., Pomraning, E., and Richards, K. J., "Multidimensional Modeling of Direct-Injection Diesel Spray Liquid Length and Flame Liftoff Length Using CFD and Parallel Detailed Chemistry," Society of Automotive Engineers Paper 2003-01-1043, 2003.

[10] Pantano, C., "Direct Simulation of Nonpremixed Flame Extinction in a Methane–Air Jet with Reduced Chemistry," *Journal of Fluid Mechanics*, Vol. 514, Aug. 2004, pp. 231–270. doi:10.1017/S0022112004000266

[11] Hawkes, E. R., Sankaran, R., Sutherland, J. C., and Chen, J. H., "Scalar Mixing in Direct Numerical Simulations of Temporally Evolving Plane Jet Flames with Skeletal CO/H2 Kinetics., *Proceedings of the Combustion Institute*, Vol. 31, No. 1, 2007, pp. 1633–1640. doi:10.1016/j.proci.2006.08.079

[12] Williams, F. A., " Progress in the Knowledge of Flamelet Structure and Extinction," *Progress in Energy and Combustion Science*, Vol. 26, Nos. 4–6, 2000, pp. 657–682. doi:10.1016/S0360-1285(00)00012-5

[13] Renard, P. H., Rolon, J. C., Thevenin, D., and Candel, S., "Dynamics of Flame/Vortex Interactions," *Progress in Energy and Combustion Science*, Vol. 26, No. 3, 2000, pp. 225–282. doi:10.1016/S0360-1285(00)00002-2

[14] Peters, N., and Williams, F. A., "Liftoff Characteristics of Turbulent Jet Diffusion Flames," *AIAA Journal*, Vol. 21, No. 3, 1983, pp. 423–429. doi:10.2514/3.8089

[15] Sripakagorn, P., Mitarai, S., Kosaly, G., and Pitsch, H., "Extinction and Reignition in a Diffusion Flame: A Direct Numerical Simulation Study," *Journal of Fluid Mechanics*, Vol. 518, Oct. 2004, pp. 231–259. doi:10.1017/S0022112004001004

[16] Buckmaster, J. D., "Edge Flames," *Progress in Energy and Combustion Science*, Vol. 28, No. 5, 2002, pp. 435–475. doi:10.1016/S0360-1285(02)00008-4

[17] Peters, N., "Numerical and Asymptotic Analysis of Systematically Reduced Reaction Schemes for Hydrocarbon Flames," *Lecture Notes in Physics*, Vol. 241, May 1985, pp. 90–109. doi:10.1007/BFb0008654

[18] Santoro, V. S., Linan, A., and Gomez, A., "Propagation of Edge Flames in Counterflow Mixing Layers: Experiments and Theory," *Proceedings of the Combustion Institute*, Vol. 28, No. 2, 2000, pp. 2039–2046.

[19] Santoro, V. S., Kyritsis, D. C., Linan, A., and Gomez, A., "Vortex-Induced Extinction Behavior in Methanol Gaseous Flames: A Comparison with Quasi-Steady Extinction," *Proceedings of the Combustion Institute*, Vol. 28, No. 2, 2000, pp. 2109–2116.

[20] Hermanns, M., Vega, M., and Linan, A., "On the Dynamics of Flame Edges in Diffusion Flame/Vortex Interactions," *Combustion and Flame*, Vol. 149, Nos. 1–2, 2007, pp. 32–48. doi:10.1016/j.combustflame.2006.12.012

[21] Yoshida, K., and Takagi, T., "Transient Local Extinction and Reignition Behavior of Diffusion Flames Affected by Flame Curvature and Preferential Diffusion," *Proceedings of the Combustion Institute*, Vol. 27, No. 1, 1998, pp. 685–692.

[22] Finke, H., and Grünefeld, G., "An Experimental Investigation of Extinction of Curved Laminar Hydrogen Diffusion Flames," *Proceedings of the Combustion Institute*, Vol. 28, No. 2, 2000, pp. 2133–2140.

[23] Amantini, G., Frank, J. H., and Gomez, A., "Experiments on Standing and Traveling Edge Flames around Flame Holes," *Proceedings of the Combustion Institute*, Vol. 30, No. 3, 2005, pp. 313–321. doi:10.1016/j.proci.2004.08.230

[24] Amantini, G., Frank, J. H., Bennett, B. A. V., Smooke, M. D., and Gomez, A., "Comprehensive Study of the Evolution of an Annular Edge Flame during Extinction and Reignition of a Counterflow Diffusion Flame Perturbed by Vortices," *Combustion and Flame*, Vol. 147, Nos. 1–2, 2006, pp. 133–149. doi:10.1016/j.combustflame.2006.05.006

[25] Peters, N., Paczko, G., Seiser, R., and Seshadri, K., "Temperature Cross-Over and NonThermal Runaway at Two-Stage Ignition of *n*-Heptane," *Combustion and Flame*, Vol. 128, Nos. 1–2, 2002, pp. 38–59. doi:10.1016/S0010-2180(01)00331-5

[26] Thevenin, D., Renard, P. H., Fiechetner, C. J., Gord, J. R., and Rolon, J. C., "Regimes of Nonpremixed Flame–vortex Interactions," *Proceedings of the Combustion Institute*, Vol. 28, No. 2, 2000, pp. 2101–2108.

[27] Oh, C. B., Lee, C. E., and Park, J., "Numerical Investigation of Extinction in a Counterflow Nonpremixed Flame Perturbed by a Vortex," *Combustion and Flame*, Vol. 138, No. 3, 2004, pp. 225–241. doi:10.1016/j.combustflame.2004.03.013

[28] Abraham, J., and Magi, V., "Exploring Velocity and Density Ratio Effects in a Mixing Layer Using DNS," Short Communication, International Journal of Computational Fluid Dynamics, Vol. 8, No. 2, 1997, pp. 147–151.

[29] Viggiano, A., and Magi, V., "A 2-D Investigation of *n*-Heptane Autoignition by Means of Direct Numerical Simulation," *Combustion and Flame*, Vol. 137, No. 4, 2004, pp. 432–443. doi:10.1016/j.combustflame.2004.03.003

[30] Anders, J. W., Magi, V., and Abraham, J., "Large-Eddy Simulation in the Near Field of a Transient Multicomponent Gas Jet with Density Gradients,"*Computers and Fluids*, Vol. 36, No. 10, 2007, pp. 1609–1620. doi:10.1016/j.compfluid.2007.03.002

[31] Bird, R. B., Stewart, W. E., Lightfoot, E. N., *Transport Phenomena*, Wiley, New York, 1960, p. 571.

[32] Lele, S. K., "Finite Difference Schemes with Spectral-Like

Resolution," *Journal of Computational Physics*, Vol. 103, No. 1, 1992, pp. 16–42.
doi:10.1016/0021-9991(92)90324-R

[33] Carnahan, B., *Applied Numerical Methods*, Wiley, New York, 1969, p. 363.

[34] Poinsot, T. J., and Lele, S. K., "Boundary Conditions for Direct Simulations of Compressible Viscous Flows," *Journal of Computational Physics*, Vol. 101, No. 1, 1992, pp. 104–129.
doi:10.1016/0021-9991(92)90046-2

[35] Seiser, R., Truett, L., Trees, D., and Seshadri, K., "Structure and Extinction of Nonpremixed *n*-Heptane Flames," *Proceedings of the Combustion Institute*, Vol. 27, No. 1, 1998, pp. 649–657.

[36] Lutz, A. E., Kee, R. J., Grcar, J. F., and Rupley, F. M., "OPPDIFF: A FORTRAN Program for Computing Opposed Flow Diffusion Flames", Sandia National Labs. Paper 96-8243, 1996.

[37] Berta, P., Puri, I. K., and Agarwal, S. K., "Structure of Partially Premixed *n*-Heptane Counterflow Flames," *Proceedings of the Combustion Institute*, Vol. 30, No. 1, 2005, pp. 447–453.
doi:10.1016/j.proci.2004.08.141

[38] Cuenot, B., and Poinsot, T., "Effects of Unsteadiness and Curvature on Diffusion Flames: Implications for Turbulent Diffusion Combustion," *Proceedings of the Combustion Institute*, Vol. 25, No. 1, 1994, pp. 1383–1390.

[39] Vervisch, L., and Poinsot, T., "Direct Numerical Simulation of Nonpremixed Turbulent Flames," *Annual Review of Fluid Mechanics*, Vol. 30, Jan. 1998, pp. 655–691.
doi:10.1146/annurev.fluid.30.1.655

[40] Moran, M. J., and Shapiro, H. N., *Fundamentals of Engineering Thermodynamics*, 4th Edition, Wiley, New York, 2000, pp. 554–555.

[41] Gopalakrishnan, V., and Abraham, J., "An Investigation of Ignition Behavior in Diesel Sprays," *Proceedings of the Combustion Institute*, Vol. 29, No. 1, 2002, pp. 641–646.

[42] Bilger, R. W., "The Structure of Turbulent Nonpremixed Flames," *Proceedings of the Combustion Institute*, Vol. 22, No. 1, 1989, pp. 475–488.

[43] Vera, M., and Linan, A., "On the Interaction of Vortex Rings with Mixing Layers," *Physics of Fluids*, Vol. 16, No. 7, 2004, pp. 2237–2254.
doi:10.1063/1.1718956

[44] Karagozian, A. R., and Marble, F. E., "Study of a Diffusion Flame in a Stretched Vortex," *Combustion Science and Technology*, Vol. 45, Nos. 1–2, 1986, pp. 65–84.
doi:10.1080/00102208608923842

[45] Gokula, H. K., and Echekki, T., "Direct Numerical Simulation of Premixed Flame Kernel-Vortex Interactions in Hydrogen–Air Mixtures," *Combustion and Flame*, Vol. 146, Nos. 1–2, 2006, pp. 155–167.
doi:10.1016/j.combustflame.2006.04.002

[46] Katta, V. R., Carter, C. D., Fiechtner, G. J., Roquemore, W. M., Gord, J. R., and Rolon, J. C., "Interaction of a Vortex with a Flat Flame Formed Between Opposing Jets of Hydrogen and Air," *Proceedings of the Combustion Institute*, Vol. 27, No. 1, 1998, pp. 587–594.

[47] Glezer, A., "The Formation of Vortex Rings," *Physics of Fluids*, Vol. 31, No. 12, 1988, pp. 3532–3542.
doi:10.1063/1.866920

[48] Dimotakis, P. E., "Turbulent Mixing," *Annual Review of Fluid Mechanics*, Vol. 37, 2005, pp. 329–356.
doi:10.1146/annurev.fluid.36.050802.122015

[49] Favier, V., and Vervisch, L., "Edge flames and Partially Premixed Combustion in Diffusion Flame Quenching," *Combustion and Flame*, Vol. 125, Nos. 1–2, 2001, pp. 788–803.
doi:10.1016/S0010-2180(00)00242-X

[50] Pitsch, H., Barths, H., and Peters, N., "Three-Dimensional Modeling of NOx and Soot Formation in DI Diesel Engines Using Detailed Chemistry Based on the Interactive Flamelet Approach," Society of Automotive Engineers Paper 96-2057, 1996.

[51] Kortschik, C., Honnet, S., and Peters, N., "Influence of Curvature on the Onset of Autoignition in a Corrugated Counterflow Mixing Field," *Combustion and Flame*, Vol. 142, Nos. 1–2, 2005, pp. 140–152.

[52] Frenklach, M., and Wang, H., " Detailed Modeling of Soot Particle Nucleation and Growth," *Proceedings of the Combustion Institute*, Vol. 23, No. 1, 1991, pp. 1559–1566.

[53] Pitsch, H., and Ihme, M., "An Unsteady Flamelet / Progress Variable Method for LES of Nonpremixed Turbulent Combustion," 43rd AIAA Aerospace Sciences Meeting and Exhibit, AIAA Paper 2004-557, Reno, NV, Jan. 2005.

[54] Amantini, G., Gomez, A., and Williams, F. A., "Application of Two-Dimensional Unsteady Flamelets to Capture Local Extinction and Reignition in Turbulent Nonpremixed Combustion," *Proceedings of the 8th Turbulent Nonpremixed Flames Workshop*, Sandia National Labs., Albuquerque, NM, 3-5 Aug. 2006, pp. 272–273.

T. Jackson
Associate Editor